

SSC-467

**INCORPORATION OF RESIDUAL STRESS
EFFECTS IN A PLASTICITY AND DUCTILE
FRACTURE MODEL FOR
RELIABILITY ASSESSMENT OF ALUMINUM
SHIP STRUCTURE**



This document has been approved
For public release and sale; its
Distribution is unlimited

SHIP STRUCTURE COMMITTEE
2013

Ship Structure Committee

RDML J.A. Servidio
U. S. Coast Guard Assistant Commandant,
Assistant Commandant for Prevention Policy
Co-Chair, Ship Structure Committee

Mr. H. Paul Cojeen
Society of Naval Architects and Marine Engineers

Mr. Christopher McMahon
Director, Office of Ship Construction
Maritime Administration

Mr. Kevin Baetsen
Director of Engineering
Military Sealift Command

Mr. Jeffrey Lantz,
Commercial Regulations and Standards for the
Assistant Commandant for Marine Safety, Security
and Stewardship
Mr.
Deputy Assistant Commandant for Engineering and
Logistics

RADM Thomas Eccles
Chief Engineer and Deputy Commander
For Naval Systems Engineering (SEA05)
Co-Chair, Ship Structure Committee

Mr. Todd Grove
Chief Technical Officer (CTO)
American Bureau of Shipping

Ms. Julie Gascon
Director Design, Equipment and Boating Safety,
Marine Safety,
Transport Canada

Dr. Neil Pegg
Group Leader - Structural Mechanics
Defence Research & Development Canada - Atlantic

Mr. Eric C. Duncan
Director, Structural Integrity and Performance Division

Dr. John Pazik
Director, Ship Systems and Engineering Research
Division

SHIP STRUCTURE SUB-COMMITTEE

AMERICAN BUREAU OF SHIPPING (ABS)

Mr. Craig Bone
Mr. Phil Rynn
Mr. Tom Ingram

MARITIME ADMINISTRATION (MARAD)

Mr. Chao Lin
Mr. Richard Sonnenschein

NAVY/ONR / NAVSEA/ NSWCCD

Mr. David Qualley / Dr. Paul Hess
Mr. Erik Rasmussen / Dr. Roshdy Barsoum
Mr. Nat Nappi, Jr.
Mr. Dean Schleicher

UNITED STATES COAST GUARD

CAPT John Mauger
Mr. Jaideep Sirkar
Mr. Chris Cleary
Mr. Frank DeBord

DEFENCE RESEARCH & DEVELOPMENT CANADA

ATLANTIC

Mr. Malcolm Smith
Dr. Layton Gilroy

MILITARY SEALIFT COMMAND (MSC)

Mr. Michael W. Touma
Mr. Jitesh Kerai

TRANSPORT CANADA

Mr. Ian Campbell
Mr. Bashir Ahmed Golam
Mr. Luc Tremblay

SOCIETY OF NAVAL ARCHITECTS AND MARINE ENGINEERS (SNAME)

Mr. Rick Ashcroft
Mr. Dave Helgerson
Mr. Alex Landsburg
Mr. Paul H. Miller

Member Agencies:

*American Bureau of Shipping
Defence Research and Development Canada
Maritime Administration
Military Sealift Command
Naval Sea Systems Command
Office of Naval Research
Society of Naval Architects & Marine Engineers
Transport Canada
United States Coast Guard*



Ship
Structure
Committee

Address Correspondence to:

COMMANDANT (CG-ENG-2/SSC)
ATTN (EXECUTIVE DIRECTOR/SHIP
STRUCTURE COMMITTEE)
US COAST GUARD
2100 2ND ST SW STOP 7126
WASHINGTON DC 20593-7126
Website: <http://www.shipstructure.org>

SSC – 467
SR – 1467

June 28, 2013

**INCORPORATION OF RESIDUAL STRESS EFFECTS IN A PLASTICITY AND DUCTILE
FRACTURE MODEL FOR RELIABILITY ASSESSMENTS OF ALUMINUM SHIP
STRUCTURE**

Despite conservative ship structure design practices to resist large plastic deformations, fatigue crack initiation and brittle fracture, cracking still occurs in ship structures under seemingly low loads. In reality these designs do not effectively account for the contribution of residual stresses which are most often introduced during fabrication welding as the weld cools, shrinks, and pulls on the surrounding metal, creating stresses that can be as high as yield. Combined with acceptable service loads, the residual stresses can exceed a material's resistance to damage resulting in crack initiation and propagation. Handling of these unknowns in the design of steel ships has been accomplished by introducing large safety factors in the design. But in order to achieve the performance requirements and advantages of new lightweight aluminum structures, these safety factors must be minimized.

This project experimentally quantifies the effect of residual stress on the fracture resistance of 5083-H1116, a marine structural aluminum alloy.

We thank the authors and Project Technical Committee for their dedication and research toward completing the objectives and tasks detailed throughout this paper and continuing the Ship Structure Committee's mission to enhance the safety of life at sea.


JOSEPH A. SERVIDIO
Rear Admiral, U.S. Coast Guard
Co-Chairman, Ship Structure Committee


T. J. ECCLES
Rear Admiral, U.S. Navy
Co-Chairman, Ship Structure Committee

1. Report No. 467	2. Government Accession No.	3. Recipient's Catalog No.	
4. Title and Subtitle Incorporation of Residual Stress Effects in a Plasticity and Ductile Fracture Model for Reliability Assessments of Aluminum Ship Structure		5. Report Date	
		6. Performing Organization Code 612	
7. Author(s) Hayden, M.J.; Gao, X.; Zhou, J.; Joyce, J.A.		8. Performing Organization Report No. SR-1467	
9. Performing Organization Name and Address Naval Surface Warfare Center, Carderock Division (NSWCCD) 9500 MacArthur Blvd West Bethesda, MD 20817		10. Work Unit No. (TRAVIS)	
		11. Contract or Grant No.	
12. Sponsoring Agency Name and Address COMMANDANT (CG-ENG-2/SSC) ATTN (SHIP STRUCTURE COMMITTEE) US COAST GUARD 2100 2ND ST SW STOP 7126 WASHINGTON DC 20593-7126		13. Type of Report Final Report	
		14. Sponsoring Agency Code CG - 5P	
15. Supplementary Notes The research completed by the above author for the Ship Structure Committee was reviewed by the Project Technical Committee for satisfactory completion of the objectives outlined in the Statement of Work developed and approved for funding by the Principal Members of the Ship Structure Committee. Sponsored by the Ship Structure Committee and its member agencies			
16. Abstract Elastic-plastic fracture toughness is measured in 5083-H116 aluminum under the influences of applied tensile residual stress and applied compressive residual stress. Finite element analyses using a calibrated I-J-J- dependent plasticity and stress triaxiality-Lode angle-dependent fracture model predicted crack initiation and extension. Comparison between experimental and predicted load-displacement data and experimental and predicted fracture surfaces support the accuracy of the model. The resulting model can inform structural assessments and fracture control plans of aluminum ship structure.			
17. Key Words fracture toughness, ductile fracture, residual stress, aluminum, finite element analysis		18. Distribution Statement National Technical Information Service U.S. Department of Commerce Springfield, VA 22151 Ph. (703) 487-4650 / www.ntis.gov	
19. Security Classif. (of this report) Unclassified	20. Security Classif. (of this page) Unclassified	21. No. of Pages	22. Price

1. Report No.	2. Government Accession No.	3. Recipient's Catalog No.	
4. Title and Subtitle INCORPORATION OF RESIDUAL STRESS EFFECTS IN A PLASTICITY AND DUCTILE FRACTURE MODEL FOR RELIABILITY ASSESSMENTS OF ALUMINUM SHIP STRUCTURE		5. Report Date	
		6. Performing Organization Code 612	
7. Author(s) M.J. Hayden, X. Gao, J. Zhou, J.A. Joyce		8. Performing Organization Report No. SR-1467	
9. Performing Organization Name and Address Naval Surface Warfare Center, Carderock Division 9500 MacArthur Blvd West Bethesda, MD 20817		10. Work Unit No. (TRAIS)	
		11. Contract or Grant No.	
12. Sponsoring Agency Name and Address COMMANDANT (CG-5212/SSC) ATTN (SHIP STRUCTURE COMMITTEE) US COAST GUARD 2100 SECOND ST SW STOP 7126 WASHINGTON DC 20593-7126		13. Type of Report Final Report	
		14. Sponsoring Agency Code CG - 5	
15. Supplementary Notes Sponsored by the Ship Structure Committee and its member agencies			
16. Abstract Elastic-plastic fracture toughness is measured in 5083-H116 aluminum under the influences of applied tensile residual stress and applied compressive residual stress. Finite element analyses using a calibrated I_1 - J_2 - J_3 -dependent plasticity and stress triaxiality-Lode angle-dependent fracture model predicted crack initiation and extension. Comparison between experimental and predicted load-displacement data and experimental and predicted fracture surfaces support the accuracy of the model. The resulting model can inform structural assessments and fracture control plans of aluminum ship structure.			
17. Key Words Fracture toughness, ductile fracture, residual stress, aluminum, finite element analysis		18. Distribution Statement Distribution unlimited, available from: National Technical Information Service U.S. Department of Commerce Springfield, VA 22151 Ph. (703) 487-4650 / www.ntis.gov	
19. Security Classif. (of this report) Unclassified	20. Security Classif. (of this page) Unclassified	21. No. of Pages	22. Price

CONVERSION FACTORS
(Approximate conversions to metric measures)

To convert from	to	Function	Value
LENGTH			
inches	meters	divide	39.3701
inches	millimeters	multiply by	25.4
feet	meters	divide by	3.2808
FORCE OR MASS			
pounds	tonnes	divide by	2204.62
pounds	kilograms	divide by	2.2046
pounds	Newtons	multiply by	4.4482
kilo pounds (kip)	Newtons	divide by	0.2248
PRESSURE OR STRESS			
pounds/inch ² (psi)	Newtons/meter ² (Pascals)	multiply by	6894.8
kilo pounds/inch ² (ksi)	mega Newtons/meter ² (mega Pascals)	multiply by	6.8947
STRESS INTENSITY			
kilo pound/inch ² inch ^{1/2} (ksi√in)	mega Newton meter ^{3/2} (MNm ^{3/2})	multiply by	1.0998
J-INTEGRAL			
kilo pound/inch	Joules/mm	multiply by	0.1753
kilo pound/inch	kilo Joules/m ²	multiply by	175.3
inch pound/inch ² (in-lb/in ²)	Joules/mm	multiply by	175.3

TABLE OF CONTENTS

1. Background	1
1.1. Introduction	1
1.2. Material Model Development	1
1.2.1. Plasticity Model	2
1.2.2. Fracture Model	3
1.3. Model Calibration for Aluminum Alloy 5083-H116	5
1.3.1. Calibration of the Plasticity Model	5
1.3.2. Calibration of the Fracture Model	8
2. Specimen and Fixture Design	10
2.1. General Analysis	12
2.2. Influence of the Depth of Indentation	12
2.3. Influence of the Indentation Position Along the Crack Path	14
2.4. Influence of the Indentation Position Normal to the Crack Plane	14
2.5. Influence of the Indentation Radius	15
2.6. Alternating Side Compression Versus Simultaneous Side Compression	16
3. Testing and Analysis	17
3.1. Analysis of Control Specimen with No Side Grooves	21
3.2. Analysis of Control Specimen with 20% Side Grooves	23
3.3. Tensile Residual Stress Testing	24
3.4. Analysis of Tensile Residual Stress Specimens	28
3.5. Compressive Residual Stress Testing	30
3.6. Analysis of Compressive Residual Stress Specimens	31
3.7. Separating the Effects of Side Compression from Plastic Damage and the Effects of Residual Stress on Fracture Toughness	34
4. Discussion	35
5. Conclusions	35
6. Implications for Ship Structure	36
7. Recommendations for Future Research	37
8. References	38
Appendix: Manufacturer Certificate for Material of This Study	2

LIST OF ILLUSTRATIONS

Figure 1. Schematics of a smooth round bar, a notched round bar, a cylindrical compression specimen, a grooved plane strain specimen and a torsion specimen used in calibration of the plasticity and fracture models.	5
Figure 2: Comparison of the numerical and experimental load versus displacement curves for the smooth tensile specimen (left) and the compression specimen (right).	7
Figure 3: Comparison of numerical and experimental data for the pure torsion specimen (a), and a torsion-tension specimen (b) and (c).	7
Figure 4. 2D failure surface (left) and 3D failure surface (right).	8
Figure 5: Schematic of compact tension specimen with side compression configurations in the applied tensile residual stress (a) and the applied compressive residual stress (b) configurations.	10
Figure 6: (a) Compact tension specimen dimensions and (b) schematic of quarter-symmetry finite element model, units in inches.	11
Figure 7: Finite element contours across the half-thickness at the specimen crack tip with (a) tensile residual stress (depression ahead of crack tip) and (b) compressive residual stress (depression behind crack tip). The crack tips are highlighted in contrasting colors and the cracks grow to the left.	11
Figure 8: Residual stress distribution ahead of the crack tip at the mid-thickness of the specimen ($z = 0$).	12
Figure 9: Residual stress distribution along crack path. Green triangles represent applied displacement of 0.005 inch and red diamonds represent applied displacement of 0.006 inch.	13
Figure 10: Residual stress distribution along crack path for different indentation locations along crack path.	13
Figure 11: Residual stress distribution along crack path for different indentation locations normal to the crack plane.	14
Figure 12: Residual stress distribution along crack path for different punch radii.	15
Figure 13: Finite element contour of the asymmetric residual stress field across the thickness at the crack tip.	16
Figure 14: (a) Schematic of side compression fixture, (b) photograph of side compression indents in compressive configuration (left), and side compression indents in tensile configuration (right).	17

Figure 15: Schematic of specimen layout, dimensions in inches.	18
Figure 16: Photographs of specimen fracture surfaces with no side grooves (top row) and 20% side grooves (bottom row). In each, the crack grows toward the bottom of the page. Ductile crack fronts are highlighted in red and net thickness due to side grooves highlighted in yellow.	20
Figure 17: Finite element mesh of the control specimen, no side grooves.	22
Figure 18: Comparison of computed and measured load-displacement curves of the control specimen, no side grooves.	22
Figure 19: Fracture surface and stress triaxiality distribution in the control specimen, no side grooves.	22
Figure 20: Fracture surface and stress triaxiality distribution in the side-grooved specimen.	24
Figure 21: Comparison of the load-displacement curves for side-grooved and plane-sided specimens.	24
Figure 22: Crack driving force J versus crack extension for control specimens and applied tensile residual stress specimens.	26
Figure 23: Photographs of fracture surfaces of applied tensile residual stress specimens that were side compressed, followed by fatigue separation; no toughness test was conducted. In each, the crack grows toward the top of the page and the extent of side compression induced crack extension is darkened by dye penetrant and indicated with arrows.	27
Figure 24: SEM micrographs of fracture surface of applied tensile residual stress specimen CT26 with 0.011 inch side compression followed by immediate fatigue (left) and a tested control specimen CT17 (right). In each, the crack grows toward the top of the page and the transition from the fatigue precrack to ductile tearing is indicated.	27
Figure 25: SEM micrograph of fracture surface of applied tensile residual stress specimen CT26 with typical cracked inclusions indicated with vertical arrows. The global crack grows toward the top of the page and the transition from the fatigue precrack to ductile tearing is indicated with horizontal arrows.	27
Figure 26: Contour plots of the residual stress normal to the crack plane, 49 kips side-compression (top) and 41 kips side-compression (bottom).	29
Figure 27: Residual stresses (σ_{22}) distributions ahead of the crack tip at the mid-plane and the specimen edge.	29

Figure 28: Crack driving force J versus crack extension for control specimens and applied compressive residual stress specimens.	32
Figure 29: Photographs of fracture surfaces of applied compressive residual stress specimens CT35 with 0.011 inch of side compression (left) and specimen CT36 with 0.003 inch of side compression (right). In each, the crack grows toward the top of the page and the edge of the fatigue precrack is indicated.	33
Figure 30: Contour plot of the residual stress normal to the crack plane at the initial notch with the crack growth direction to the right (left) and plot of the variation of residual stress (σ_{22}) with the distance in the crack growth direction (right).	33
Figure 31: Comparisons of the computed and measured load-displacement curves for applied tensile residual stress (left) and applied compressive residual stress (right).	33
Figure 32: Load-displacement response comparing FEA of applied tensile residual stress specimens with the control specimen to isolate the effect of damage from residual stress.	34

LIST OF TABLES

Table 1: Test matrix	19
----------------------	----

1. Background

1.1. Introduction

Ship structures are conservatively designed to resist large plastic deformation, fatigue crack initiation due to worst case cyclic loading, and brittle fracture. Despite conservative design practices, cracking still occurs in ship structure under seemingly low loads.

In reality, these designs do not effectively account for the contribution of residual stresses. Residual stresses are commonplace in welded structure and are concentrated near welds and geometric discontinuities. They can be introduced as early as the mill during processing. They can be introduced during forming and fit-up. Most often they are introduced during fabrication welding as the weld cools, shrinks, and pulls on the surrounding metal, creating stresses that can be as high as yield. In combination with acceptable service loads, residual stresses can exceed a material's resistance to damage, causing the initiation of cracks and the enhancement of their growth in a structure. Safety factors have served the naval architect well in handling these unknowns in the design of steel ships, but must be reduced to meet the performance requirements of new lightweight aluminum structures.

This effort aims to experimentally demonstrate that residual stresses affect crack initiation and growth; quantify the effect of residual stress on fracture resistance of 5083-H116, a marine structural aluminum alloy; and extend a computational material model to predict the effects of residual stress on fracture toughness.

The approach presented involves the introduction of residual stresses into laboratory fracture toughness specimens machined from a 5083-H116 aluminum plate. Three configurations were tested: specimens with no applied residual stress act as a control, specimens with applied tensile residual stress, and specimens with applied compressive residual stress. As it is difficult to prevent residual stresses in a material during construction welding, it is also difficult to control them in a weldment for research purposes. One technique developed by Mahmoudi et al. [4] for introducing such residual stresses is the controlled application of local compression to the point of permanent set to the sides of a test specimen cut from the material of interest. Subsequent computational analysis of the mechanical testing employs a plasticity and ductile fracture model, accounts for the equivalent fracture strain introduced by the pretest compression, and quantifies the internal stress field.

This effort focuses on quantifying the effect of residual stress on fracture in base material. Future efforts can apply these methodologies to welds.

1.2. Material Model Development

To date, an overwhelming majority of structural analyses employ the classical J_2 plasticity theory to describe the plastic response of metallic alloys. This theory assumes hydrostatic stress and the third invariant of the stress deviator do not affect the plastic behavior. However, increasing experimental evidence shows that the assumptions made in the J_2 plasticity theory are invalid for

many materials. Gao et al. [1, 2] noticed that the plastic response of a 5083 aluminum alloy is stress-state dependent and proposed an I_1 - J_2 - J_3 plasticity model.

The equivalent fracture strain is often used as a ductile fracture criterion and it is widely accepted that its value depends on the stress triaxiality [3]. However, recent studies demonstrate that the stress triaxiality alone cannot sufficiently characterize the effect of stress state on ductile fracture. Gao et al. [1] developed a stress-state dependent ductile fracture model, where the equivalent fracture strain is expressed as a function of both the stress triaxiality and the third invariant of the stress deviator (related to the Lode parameter).

1.2.1. Plasticity Model

The isotropic, stress state dependent plasticity model is formulated in terms of the invariants of the stress tensor. Let σ_{ij} be the stress tensor and σ_1 , σ_2 and σ_3 be the principal stress values. I_1 represents the first invariant of the stress tensor and the summation convention is adopted for repeated indices. The hydrostatic stress (or mean stress) can be expressed as:

$$\sigma_h = \frac{1}{3}I_1 = \frac{1}{3}\sigma_{ii} = \frac{1}{3}(\sigma_1 + \sigma_2 + \sigma_3) \quad (1)$$

Let σ'_{ij} be the stress deviator tensor and σ'_1 , σ'_2 and σ'_3 be its principal values, i.e.

$$\sigma'_{ij} = \sigma_{ij} - \sigma_h \delta_{ij} \quad (2)$$

where δ_{ij} represents the Kronecker delta. It is obvious that the first invariant of the stress deviator tensor is zero. The second and third invariants of the stress deviator tensor are defined as:

$$J_2 = \frac{1}{2}\sigma'_{ij}\sigma'_{ji} = -(\sigma'_1\sigma'_2 + \sigma'_2\sigma'_3 + \sigma'_3\sigma'_1) = \frac{1}{6}[(\sigma_1 - \sigma_2)^2 + (\sigma_2 - \sigma_3)^2 + (\sigma_3 - \sigma_1)^2]$$

$$J_3 = \det(\sigma'_{ij}) = \frac{1}{3}\sigma'_{ij}\sigma'_{jk}\sigma'_{ki} = \sigma'_1\sigma'_2\sigma'_3 \quad (3)$$

For isotropic materials, the general forms of the yield function (F) and the flow potential (G) are expressed as functions of I_1 , J_2 and J_3 . Equation (4) describes the yield condition and the flow rule

$$F(I_1, J_2, J_3) - \bar{\sigma} = 0; \quad \dot{\epsilon}_{ij}^p = \dot{\lambda} \frac{\partial G(I_1, J_2, J_3)}{\partial \sigma_{ij}} \quad (4)$$

where $\bar{\sigma}$ is the hardening parameter, $\dot{\epsilon}_{ij}^p$ are the rates of the plastic strain components and $\dot{\lambda}$ is a positive scalar called the plastic multiplier.

The following first order homogeneous function is used to define the yield function (F)

$$F = c_1 (a_1 I_1^6 + 27 J_2^3 + b_1 J_3^2)^{1/6} \quad (5)$$

where a_1 and b_1 are material constants and c_1 is determined by substituting the uniaxial condition into (5) so that the equivalent stress defined by $\sigma_e = F$ equals the applied stress.

$$c_1 = \left(a_1 + \frac{4}{729} b_1 + 1 \right)^{-1/6} \quad (6)$$

The flow potential (G) takes a similar form:

$$G = c_2 (a_2 I_1^6 + 27 J_2^3 + b_2 J_3^2)^{1/6}; c_2 = (a_2 + 4b_2 / 729 + 1)^{-1/6} \quad (7)$$

If the flow potential and the yield function are identical, i.e., $F = G$, a material is said to follow the associated flow rule. Furthermore, if $a_1 = b_1 = a_2 = b_2 = 0$, the plasticity model degenerates to the formulation of classical J_2 -flow theory and σ_e becomes the von Mises equivalent stress.

The hardening parameter depends on the strain history. By enforcing the equivalence of plastic work,

$$\bar{\sigma} \dot{\bar{\varepsilon}}^p = \sigma_{ij} \dot{\varepsilon}_{ij}^p \quad (8)$$

the equivalent plastic strain increment can be defined as:

$$\dot{\bar{\varepsilon}}^p = \sigma_{ij} \dot{\varepsilon}_{ij}^p / \bar{\sigma} \quad (9)$$

Therefore, the hardening behavior can be described by a stress versus plastic strain relation $\bar{\sigma}(\bar{\varepsilon}^p)$, where $\bar{\varepsilon}^p = \int \dot{\bar{\varepsilon}}^p dt$.

1.2.2. Fracture Model

The cumulative strain damage models assume that the damage toward eventual fracture is due to the plastic deformation history and the equivalent fracture strain depends on the stress state subjected by the material. Here a damage parameter, D , is introduced and given by

$$D = \int_0^{\bar{\varepsilon}^p} \frac{d\bar{\varepsilon}^p}{\varepsilon_f(\sigma)} \quad (10)$$

with ε_f being the failure strain under the current stress state characterized by two parameters T^* and ξ defined as

$$T^* = \frac{\sigma_h}{\sigma_e}, \quad \xi = \frac{27 J_3}{2 \sigma_e^3} \quad (11)$$

where T^* is the stress triaxiality ratio and ξ is related to the Lode angle, θ , through $\xi = \cos(3\theta + \pi/2)$. Therefore:

$$\varepsilon_f(\sigma) = \varepsilon_f(T^*, \xi) \quad (12)$$

Under proportional loading and if T^* and ξ remain unchanged during the loading history, when the equivalent plastic strain, $\bar{\varepsilon}^p$, reaches the critical value ε_f , D will equal one. For general cases, when the cumulative damage according to (10) reaches one, ductile failure occurs.

In (12), if ξ is a constant, ε_f becomes a function of T^* only. It is well documented that the ductility of metals increases when the material is subjected to hydrostatic pressure. Here an

exponentially decaying function having the same form as the Johnson-Cook fracture model [16] is used to describe the dependency of ε_f on T^*

$$\varepsilon_f^{\xi=\text{const.}} = [A + B \exp(C \cdot T^*)] \quad (13)$$

where A , B and C are material constants to be calibrated using experimental data.

The Lode angle distinguishes the deviatoric stress state and it is mathematically convenient to use the parameter ζ defined in (11), whose range is from -1 to 1, to quantify the Lode angle. Wilkins et al. [6] was first to introduce the effect of Lode angle on ductile fracture, where the function $\varepsilon_f(T^*, \zeta)$ was taken to be symmetric with respect to ζ . Here we follow Xue and Wierzbicki [7] and assume $\varepsilon_f(T^*, \zeta)$ take the following form

$$\varepsilon_f(T^*, \zeta) = \varepsilon_f^{\xi=1}(T^*) - (\varepsilon_f^{\xi=1}(T^*) - \varepsilon_f^{\xi=0}(T^*)) [1 - (1 - |\zeta|^n)^{1/n}] \quad (14)$$

where a symmetric function of ζ is used to interpolate the value of ε_f between two bounding values $\varepsilon_f^{\xi=1}$ and $\varepsilon_f^{\xi=0}$. The two bounding curves, $\varepsilon_f^{\xi=1}(T^*)$ and $\varepsilon_f^{\xi=0}(T^*)$ given by (15), can be calibrated by conducting simple mechanical tests: $\zeta=1$ for notched, round tensile specimens and $\zeta=0$ for flat-grooved plates under tension and the thin-walled torsion specimen. Calibration of parameter n requires performing additional tests using specimens having ζ values between zero and one, which can be done by conducting combined torsion-tension tests of thin-walled cylindrical specimens.

$$\varepsilon_f^{\xi=1} = [A_1 + B_1 \exp(C_1 \cdot T^*)], \quad \varepsilon_f^{\xi=0} = [A_2 + B_2 \exp(C_2 \cdot T^*)] \quad (15)$$

Fracture is assumed to have initiated at a material point once the failure criterion is reached. The post-initiation softening process needs to be considered in order to model crack propagation. As illustrated by Li et al.[8], because the finite element has a finite size, additional work is needed to propagate the crack through the element, i.e., the element gradually loses its strength as crack grows through it. A mesh-independent, post-initiation material degradation model based on an effective plastic displacement (u_f) is available in Abaqus [9] and is adopted in this study. The element is removed when it is fully degraded (stresses being reduced to zero).

The plasticity and ductile fracture models described above are implemented into Abaqus/Explicit via a user defined subroutine VUMAT following the procedures developed by Kim and Gao [10] and Gao et al.[2].

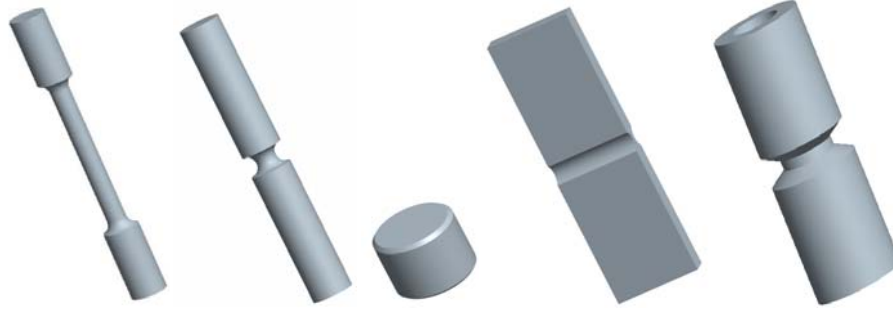


Figure 1. Schematics of a smooth round bar, a notched round bar, a cylindrical compression specimen, a grooved plane strain specimen and a torsion specimen used in calibration of the plasticity and fracture models.

1.3. Model Calibration for Aluminum Alloy 5083-H116

The plasticity and ductile fracture models described above are calibrated for an aluminum alloy 5083-H116. All calibration specimens are machined from a 1 inch thick plate. The manufacturer material certificate is presented in the Appendix. Tensile axes were oriented transversely to the rolling direction. Round specimens were turned with low stress machining procedures and rectangular specimens were electro-discharge machined. All tests are performed at room temperature and are considered to be quasi-static. The test matrix includes smooth and notched round tensile bars, cylindrical compression specimens, grooved plane strain specimens and the Lindholm-type specimen subjected to different tension-torsion ratios. Detailed descriptions of specimen geometries and finite element modeling can be found in [1, 2].

1.3.1. Calibration of the Plasticity Model

The equivalent stress-strain relation (true stress versus logarithm strain) is obtained by the uniaxial tension test, which can be described by a power-law hardening relation

$$\begin{aligned} \varepsilon &= \frac{\sigma}{E} && \text{when } \sigma \leq \sigma_0 \\ \varepsilon &= \frac{\sigma_0}{E} \left(\frac{\sigma}{\sigma_0} \right)^{1/N} && \text{when } \sigma > \sigma_0 \end{aligned} \quad (16)$$

with $E = 9.9$ msi, $\sigma_0 = 28.8$ ksi, $\nu = 0.3$, and $N = 0.155$.

The pressure dependent parameters can be calibrated by considering cylindrical compression specimens and uniaxial tensile specimens. Figure 2 compares the numerical predictions and the experimental measurements for the smooth tensile specimen (left) and the compression specimen (right). The experimental data are represented by black thin lines while the finite element result is represented by a red thick line. Using the stress strain data obtained from uniaxial tensile test, the predicted load-displacement curve of the cylindrical compression specimen fits well with the test data as shown in Figure 2 (right), which indicates the plasticity behavior of this material has no pressure dependency, thus a_1 and a_2 are set to zero.

Torsion and tension specimens exhibit different Lode parameters, thus can be used to examine the J_3 dependency. The simulation of a pure torsion test using a stress-strain curve from a uniaxial tensile test and the J_2 -plasticity model over-predicted the torque versus twist angle responses, as shown in the dotted red line of Figure 3 (a). This indicates that the plastic response is J_3 dependent. It is found that parameter b_1 has a strong effect on the predicted torque versus twist angle response of the torsion specimen while parameter b_2 has a strong effect on the predicted axial force-displacement response of the torsion-tension specimen. The final calibrated material constants are $a_1 = a_2 = 0$, $b_1 = -60.75$ and $b_2 = -50$. Figure 3 (b) and (c) compare the predicted and measured torque versus twist angle and axial force-displacement responses and show excellent agreement.

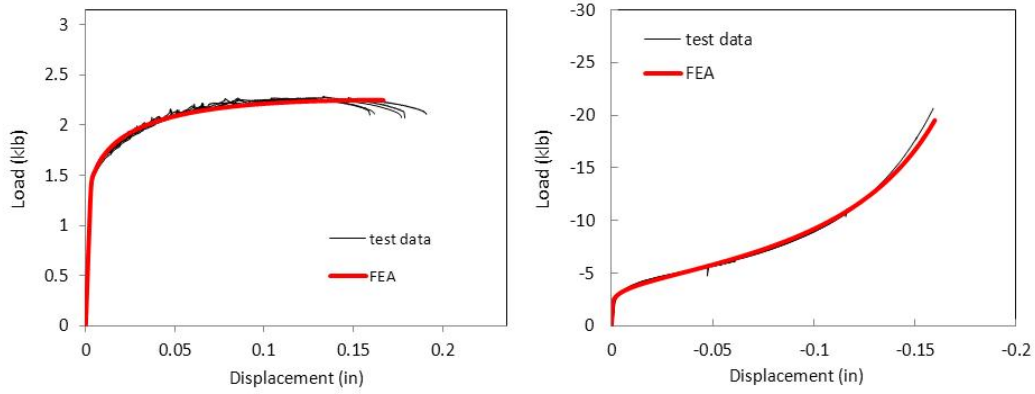


Figure 2: Comparison of the numerical and experimental load versus displacement curves for the smooth tensile specimen (left) and the compression specimen (right).

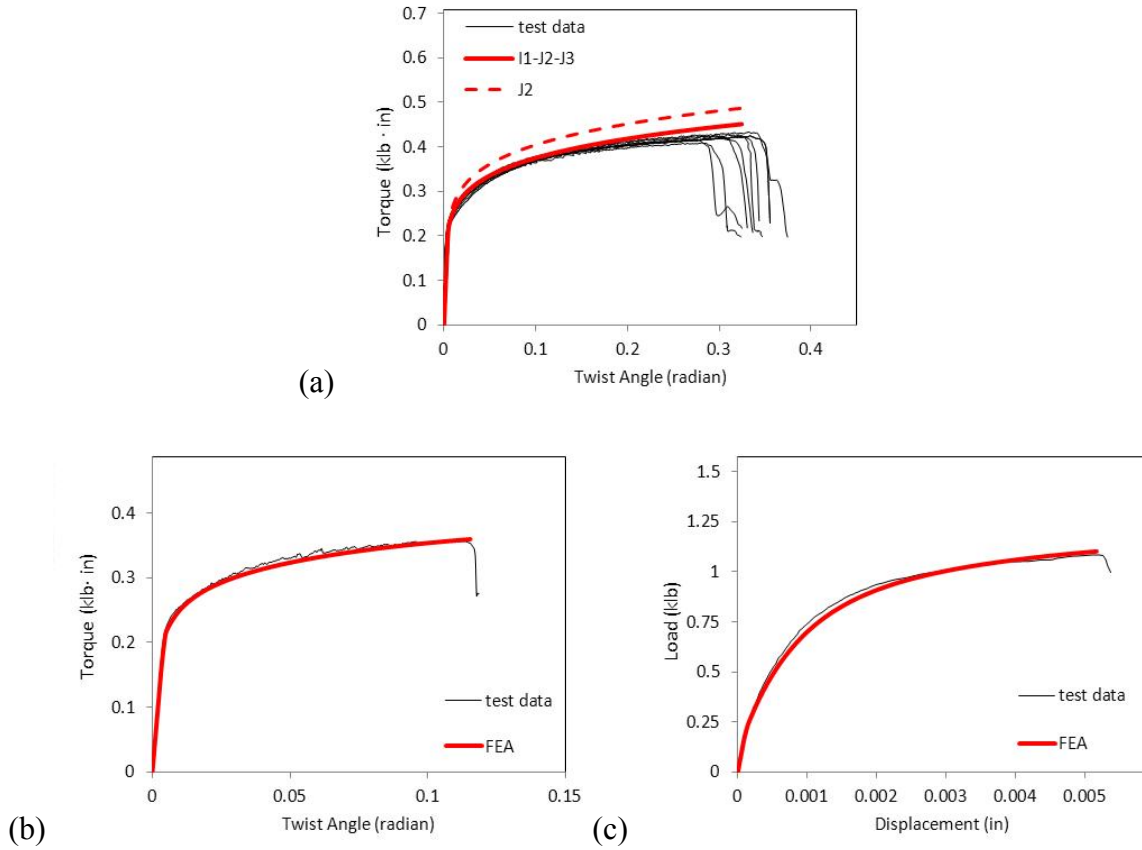


Figure 3: Comparison of numerical and experimental data for the pure torsion specimen (a), and a torsion-tension specimen (b) and (c).

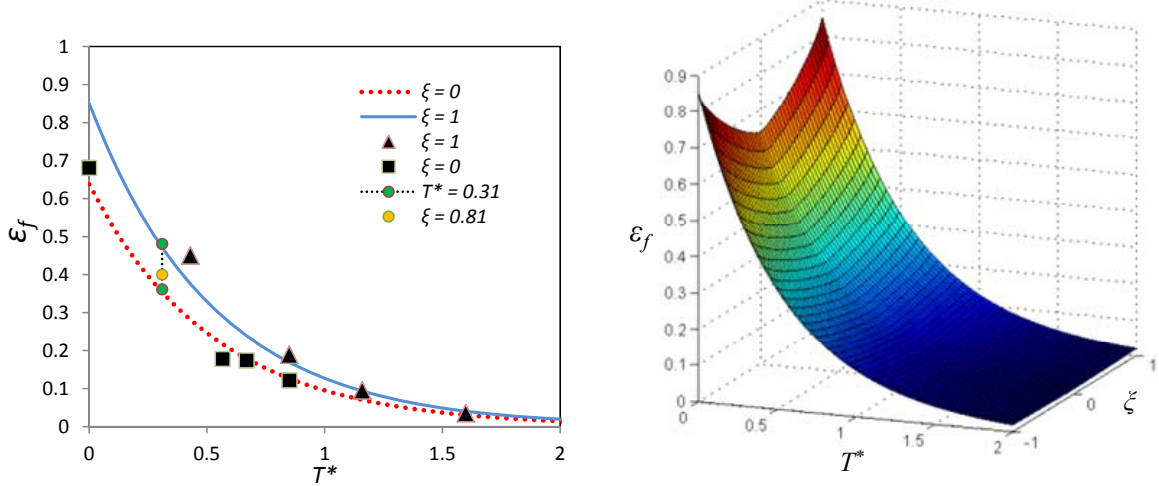


Figure 4. 2D failure surface (left) and 3D failure surface (right).

1.3.2. Calibration of the Fracture Model

As described above, parameters in (14) can be calibrated using experimental data. However, since both T^* and ξ may vary slightly in the specimen during the loading history [2], the average values, given by (17), will be used.

$$T_{av}^* = \frac{1}{\varepsilon_f} \int_0^{\varepsilon_f} T^* d\varepsilon^p; \quad \xi_{av} = \frac{1}{\varepsilon_f} \int_0^{\varepsilon_f} \xi d\varepsilon^p \quad (17)$$

Using the calibrated I_1 - J_2 - J_3 plasticity model, the load-displacement response of each tested specimen can be computed. The sudden load drop on the measured load-displacement curve designates fracture initiation. By comparing the computed and measured load-displacement curves, the increment number when fracture initiates can be determined. The histories of stress triaxiality, Lode parameter, and plastic strain increment of the critical element are output and T_{av}^* and ξ_{av} are calculated according to (17).

For asymmetric tensile specimens, including smooth round bar and all notched round bars, ξ in the center element equals to 1 and T^* varies with the notch radius. For grooved plane strain specimens, ξ in the center element equals to 0 and T^* varies with the groove radius. For the Lindholm-type specimen subjected to pure torsion, both ξ and T^* equal to zero in the gage section. For the Lindholm-type specimen subjected to combined torsion and tension, ξ and T^* in the gage section vary with the imposed torsion-tension ratio.

Using the failure strain data obtained from $\xi = 1$ and $\xi = 0$ specimens, parameters in (15) can be calibrated. The calibrated values are $A_1=0$, $B_1=0.85$, $C_1=-1.9$, $A_2=0$, $B_2=0.64$ and $C_2=-1.9$. The ε_f versus T^* curves for these two cases are plotted in Figure 4 (left). As can be seen, for both cases the failure strain decreases dramatically as the stress triaxiality increases. The difference between the two curves indicates the Lode angle dependence, although it is not very strong for this material. Using the two ε_f versus T^* curves and the torsion-tension data, which have ξ values between 0 and 1, the shape parameters n can be determined. The orange circular symbol in

Figure 4 (left) shows a data point obtained from a torsion-tension specimen having $\xi = 0.81$ and $T^* = 31$. The calibrated shape parameter for this material is $n = 1.31$.

After the parameters in (14) are calibrated, the 3D failure surface in the space of ξ and T^* is fully defined. Figure 4 (right) shows the 3D failure locus by using the calibrated parameters, $A_1 = 0$, $B_1 = 0.85$, $C_1 = -1.9$, $A_2 = 0$, $B_2 = 0.64$, $C_2 = -1.9$, and $n = 1.31$.

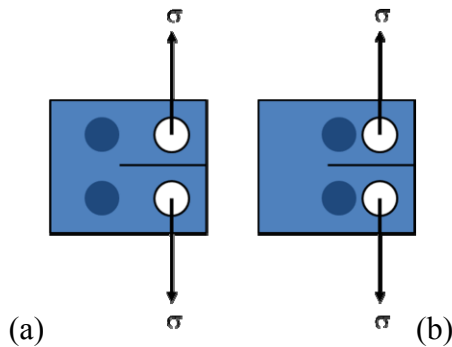


Figure 5: Schematic of compact tension specimen with side compression configurations in the applied tensile residual stress (a) and the applied compressive residual stress (b) configurations.

2. Specimen and Fixture Design

The basic specimen design utilized in this study to measure the fracture toughness of as-received plate and residual-stress induced plate is a compact tension specimen modified from the standard specified in ASTM-E1820 [5]. Residual stresses are introduced into the specimen by compressing the two faces with cylindrical punches to produce a pair of permanent circular depressions on both faces of the specimen. A residual stress field at the crack tip can be tailored by varying the position of the set of depressions relative to the crack tip. Mahmoudi et al. [4] demonstrated the adequacy of this method in 2XXX aluminums and verified residual stress calculations using X-ray techniques.

Instead of a single indents located directly on the crack path, pairs of indents straddling the crack path were chosen as illustrated in Figure 5. Indents located directly on the crack path would initiate material microstructural damage in the crack path, adding an undesirable component to the toughness measurements. Indents straddling the crack path would presumably not damage the underlying microstructure in the crack path and allow for only the resulting residual stress to influence the toughness. Unfortunately during the testing, microstructural damage was observed in the crack path in some specimens. This is detailed in a later section.

A series of finite element analyses were conducted to determine the location and amount of side compression to be applied to achieve near-yield residual stress fields for the tensile and compressive residual stress configurations. The I_1 - J_2 - J_3 plasticity model and the Lode parameter-dependent ductile fracture model were calibrated for 5083-H116 [1] and utilized in the finite element models of each specimen configuration.

A quarter-symmetry finite element model of the specimen was generated. Figure 6 shows the model dimensions with a half thickness of 0.25 inch. The 3D specimen model was meshed with C3D8R elements, a friction coefficient of 0.001 (almost frictionless), and was executed with Abaqus/Explicit. The following analyses calculate the residual stresses normal to the crack plane as they are distributed along the crack path for the main parameters of side compression geometry and placement. The intent of these analyses was to determine the optimal values for the punch radius, applied depth, x- and, y- position so that the resulting residual stress was

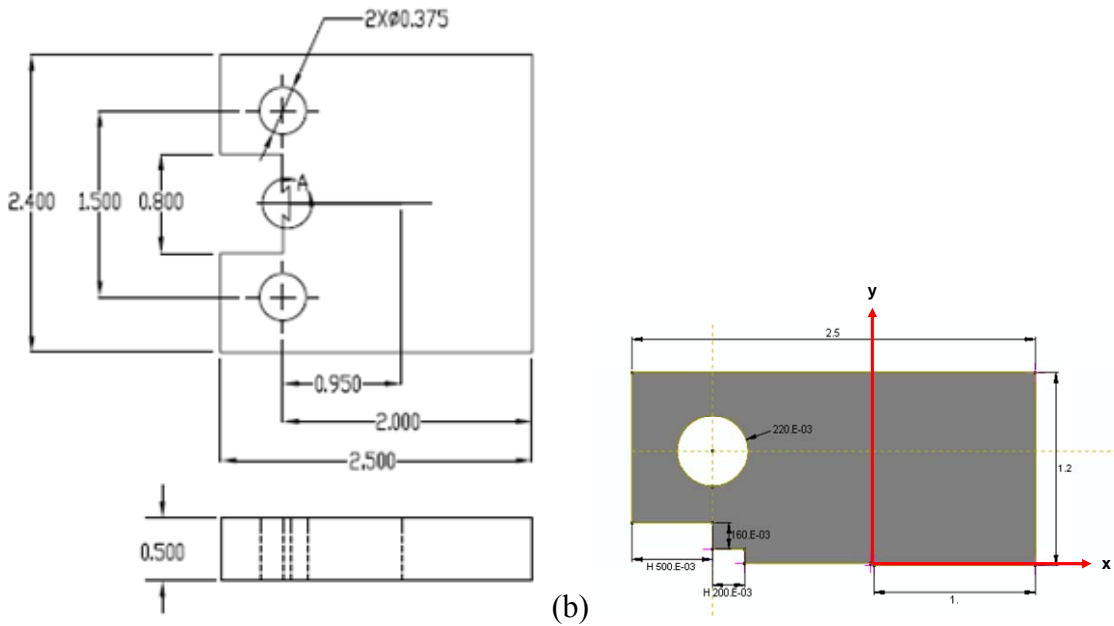


Figure 6: (a) Compact tension specimen dimensions and (b) schematic of quarter-symmetry finite element model, units in inches.

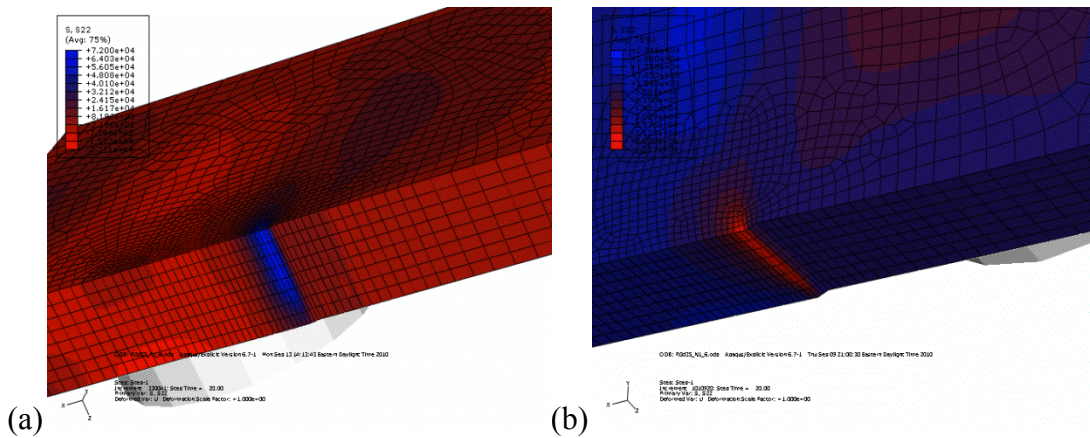


Figure 7: Finite element contours across the half-thickness at the specimen crack tip with (a) tensile residual stress (depression ahead of crack tip) and (b) compressive residual stress (depression behind crack tip). The crack tips are highlighted in contrasting colors and the cracks grow to the left.

maximized over the largest length along the crack path. Maximizing the residual stress distribution in the specimens with the side compression will overshadow any existing residual stresses in the as-received plate and will provide a greater contrast when comparing the toughness with that of the un-compressed specimens.

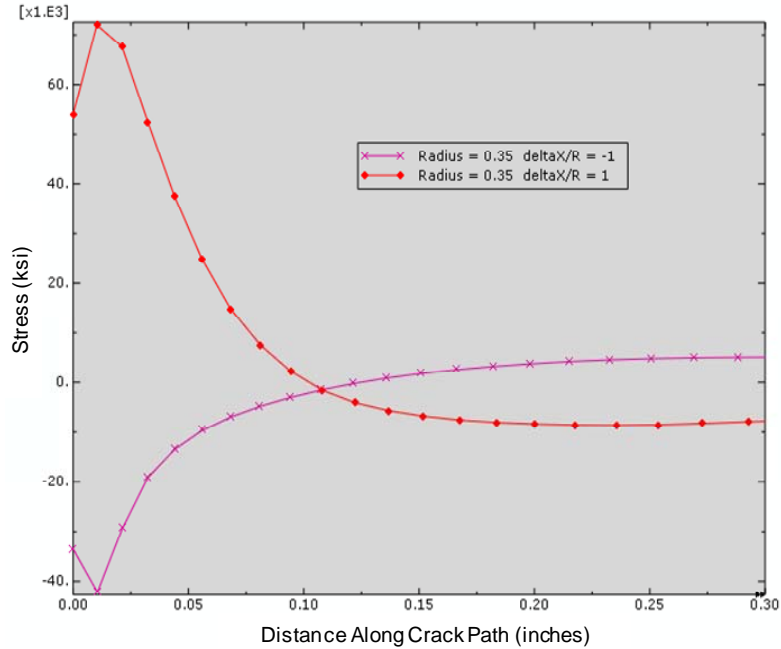


Figure 8: Residual stress distribution ahead of the crack tip at the mid-thickness of the specimen ($z = 0$).

2.1. General Analysis

In general, side compression ahead of the crack tip generates positive (tensile) residual stress at crack tip region, while side compression behind the crack tip generates negative (compressive) residual stress at the crack tip region. Finite element analyses were conducted using a punch radius of 0.35 inches, $\frac{\delta_x}{R} = 1$ and $-\frac{\delta_y}{R} = 1.2$, and a punch displacement of 0.006 inch, where δ_x and δ_y are the distances from the punch center to the crack tip and R is the radius of the punch. Residual stress contours are shown in Figure 7, where red represents negative (compressive) stress while blue represents positive (tensile) stress.

Figure 8 illustrates the decay of residual stress magnitude as the distance from crack tip increases. The level of high residual stresses in both tension and compression is confined to a small region close to the crack tip, within about 0.05 inch from the crack tip.

2.2. Influence of the Depth of Indentation

In this analysis, the punch radius was 0.35 inch, $\frac{\delta_x}{R} = 1$, and $\frac{\delta_y}{R} = 1.2$. When the punch applies a displacement of 0.006 inch, the average indentation depth after punch release is 0.005 inch corresponding to 2% combined indentation over the specimen thickness. When the punch applies a displacement of 0.005 inch, the average indentation depth becomes 0.004 inch, 1.6% combined indentation over the specimen thickness. Figure 9 shows the residual stress distribution in the mid-plane of the specimen (at $z = 0$). The difference of the resulting residual stress distribution with applied displacements of 0.005 inch and 0.006 inch is not significant. A

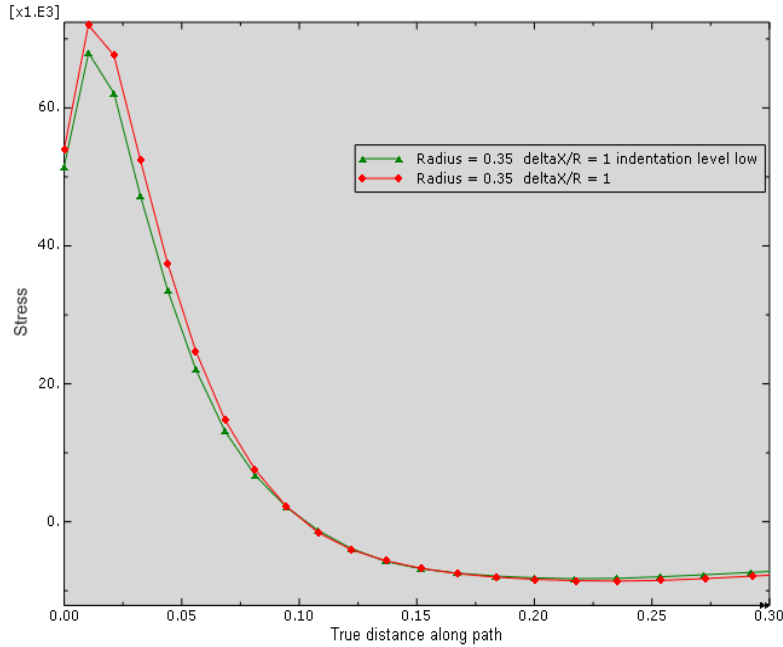


Figure 9: Residual stress distribution along crack path. Green triangles represent applied displacement of 0.005 inch and red diamonds represent applied displacement of 0.006 inch.

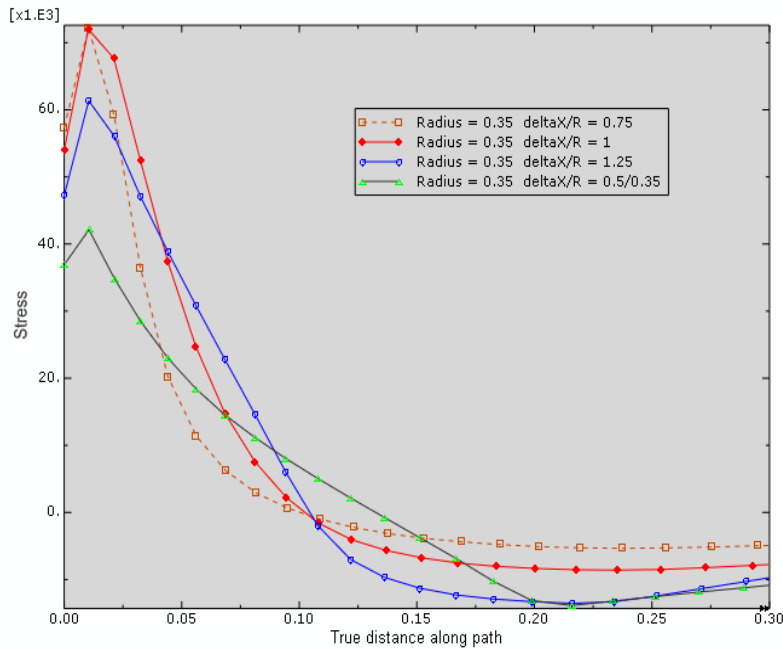


Figure 10: Residual stress distribution along crack path for different indentation locations along crack path.

depth of 0.006 inch per side was targeted, but in practice, only an average of 0.005 inch per side (0.010 inch total) was achieved by using the full capacity of the press.

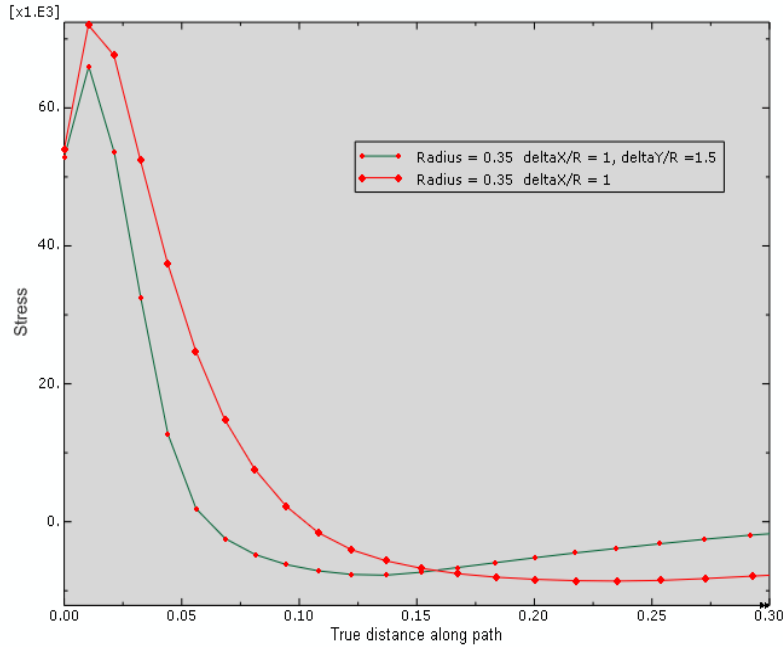


Figure 11: Residual stress distribution along crack path for different indentation locations normal to the crack plane.

2.3. Influence of the Indentation Position Along the Crack Path

In this analysis the punch radius is held constant at 0.35 inch, the punch position in y-direction $\frac{\delta_y}{R}$ is 1.2, and the applied side compression displacement at the punch is 0.006 inch. The punch position $\frac{\delta_x}{R}$ along the crack path is analyzed at values of 0.75, 1, 1.25, and 1.43. Figure 10 shows the residual stress distributions for the different punch positions. A position of $\frac{\delta_x}{R} = 1$ was targeted for the applied tensile residual stress and $\frac{\delta_x}{R} = -1$ for the applied compressive residual stress in the experiments because they induce a higher residual stress level than the other $\frac{\delta_x}{R}$ values analyzed over the region nearest the crack tip.

2.4. Influence of the Indentation Position Normal to the Crack Plane

In this analysis, the punch radius was held constant at 0.35 inch, the punch position in along the crack path was held constant at $\frac{\delta_x}{R} = 1$, and the applied displacement at the punch was held constant at 0.006 inch. Two different values of $\frac{\delta_y}{R}$ are considered, 1.5 and 1.2. Figure 11 demonstrates that when the indentation is closer to the crack plane, the resulting residual stress becomes larger and the length of the high residual stress region becomes larger. A $\frac{\delta_y}{R}$ value of 1.2 was targeted for the experiments.

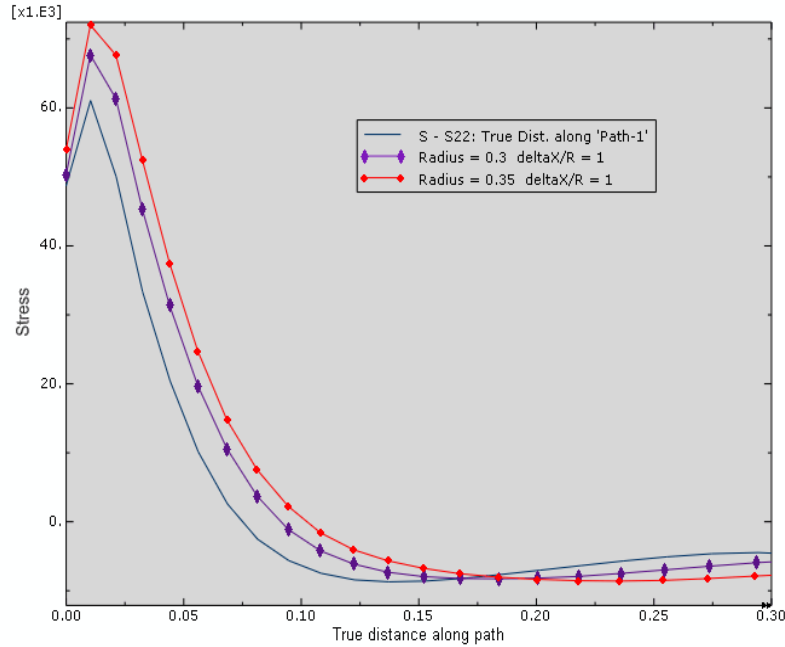


Figure 12: Residual stress distribution along crack path for different punch radii.

2.5. Influence of the Indentation Radius

This analysis was conducted to determine the punch size that would impart a desirable high residual stress field while maintaining the integrity of the compact tension specimen without exceeding the load capacity of the press. In this analysis, the punch position was fixed at $\frac{\delta_x}{R} = 1$ and $\frac{\delta_y}{R} = 1.2$ and the applied punch displacement was 0.006 inch. Three different punch radii were considered, 0.35 inch, 0.30 inch, and 0.25 inch. The geometry of the specimen limits the maximum size of the punch. Figure 12 demonstrates that a larger punch radius results in higher peak residual stress and wider region of the positive residual stress region. The radius of the punches chosen to compress the specimens is 0.35 inches.

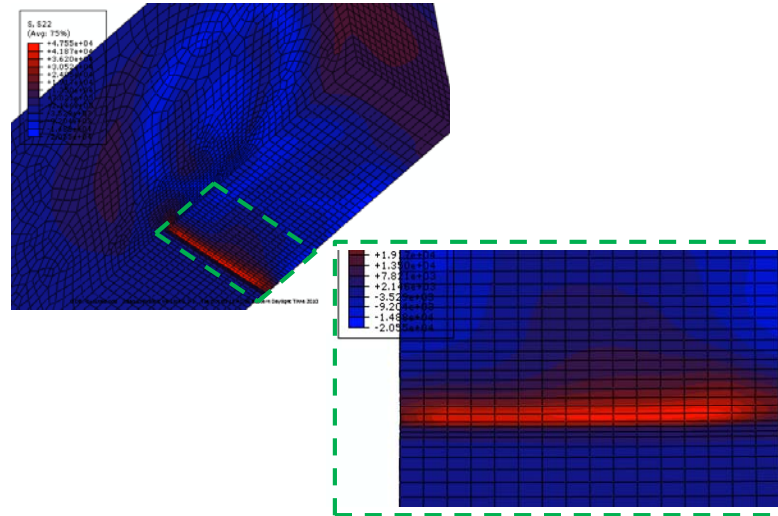


Figure 13: Finite element contour of the asymmetric residual stress field across the thickness at the crack tip.

2.6. Alternating Side Compression Versus Simultaneous Side Compression

In compressing the specimens, should one side be compressed, the specimen reversed, then the other side compressed (alternating compression) or should both sides be compressed at the same time (simultaneous compression)? A half specimen, finite element model was generated and the analysis of the alternating process was conducted in two steps, one side was compressed producing a plastic depression of the loaded surface, then the other side was compressed. The second compression distorted the plastic deformation caused by the first compression and the resulting residual stress field was found not to be uniform through the thickness, despite both sides being compressed the same amount. Figure 13 shows the crack tip and the asymmetric residual stress field across the thickness. The final depth of the indentation is not the same for both sides. Based on these results an apparatus was developed to side compress both surfaces of the specimen simultaneously. All side compression of specimens was performed in parallel using this apparatus to ensure a uniform residual stress field through the thickness.

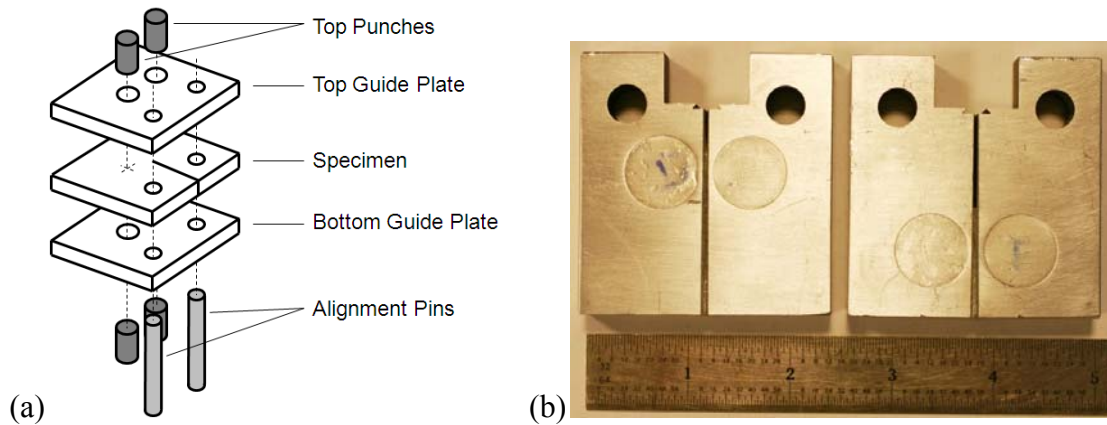


Figure 14: (a) Schematic of side compression fixture, (b) photograph of side compression indents in compressive configuration (left), and side compression indents in tensile configuration (right).

3. Testing and Analysis

Fixtures were manufactured for both $\frac{\delta_x}{R} = 1$ (tension) and $\frac{\delta_x}{R} = -1$ (compression) configurations. Figure 14 (a) depicts the side compression of a specimen. The specimen is sandwiched between two guide plates. The guide plates are aligned with the specimen by threading two pins through one guide plate, the pin loading holes of the specimen, and through the other guide plate. These guide pins ensure consistency in locating the side compression indentations between specimens. Two hardened steel side compression punches (one on either side of the crack plane) were placed in the top guide plate and two mating punches were placed in the bottom guide plate. The punches were effectively rigid in comparison to the aluminum specimens. Once assembled, load was applied to the punches until the desired plastic set was achieved.

The side compression fixtures were exercised on trial specimens to gain experience in accurately achieving the desired amount of side compression. The photograph of Figure 14 (b) depicts side-grooved specimens with indents in the compressive and tensile residual stress configurations, respectively. Side compression depths were repeatedly achieved within a 0.001 inch tolerance. Figure 15 depicts the layout of specimens from the same 1 inch thick 5083-H116 plate used in model calibration. The quasi-static testing of seven standard tensile specimens from this plate oriented in the transverse direction measured an average yield strength of 32.3 ksi, an average ultimate strength of 46.7 ksi, an average elongation of 17.3%, and an average reduction in area of 16.3%. Compact tension specimens of this study were oriented with the crack plane in the T-L direction and were located at least 6 inches from the transverse edges.

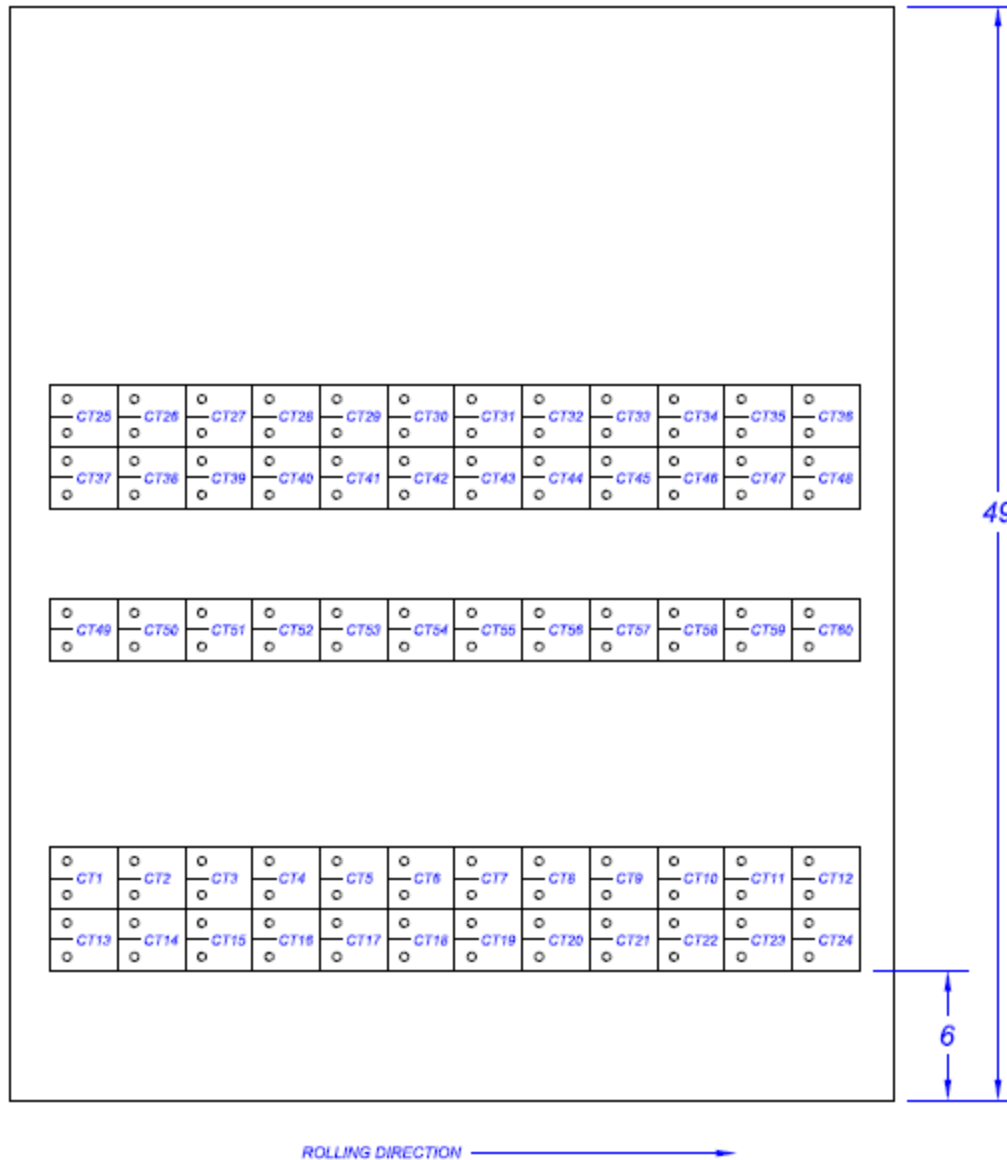


Figure 15: Schematic of specimen layout, dimensions in inches.

Table 1 presents the testing completed in this effort. Unless otherwise indicated, the testing described in this report was conducted in the following manner. The notch of each specimen was nominally fatigue precracked 0.050 inch from an initial length of 0.950 inch to a total sharp crack length of 1.000 inch under a decreasing applied stress intensity K regime from an initial maximum applied cyclic stress intensity K_{max} of 10 ksi $\sqrt{\text{in}}$ with a stress ratio of 0.1. The final K_{max} was about 8 ksi $\sqrt{\text{in}}$ for each specimen. Side grooves were machined at a depth of 0.050 inch per side on each specimen corresponding to 20% of the total specimen thickness. Residually stressed specimens were fitted into the jig and side compressed. Testing was conducted according to ASTM E1820 [5] while employing the compliance method of crack length measurement. Following testing, specimens were fatigued through complete separation so that the fracture surfaces could be measured and examined. Fatigue produces a smoother fracture surface than ductile fracture, enabling differentiation with the portion of the fracture surface

Table 1: Test matrix

Specimen	Side Compression Applied Load (kip)	Total Side Compression (avg between two indents) (in)	Nominal Total Side Groove Depth (in)	Comments	COMPLIANCE Crack Extension (in)	OPTICAL Crack Extension (in)	J_{Ic} (in-lb/in ²)
CT1	49.1	0.0080	0.000	Effect of side grooves			
CT3	49.1	0.0060	0.050	Effect of side grooves			
CT4	49.1	0.0070	0.100	Effect of side grooves	0.232	0.282	9.0
CT6	---	---	0.050	Effect of side grooves			
CT7	---	---	0.100	Effect of side grooves	0.230	0.248	64.0
CT8	---	---	0.100	Effect of side grooves	0.273	0.283	58.0
CT9	49.1	0.0080	0.000	Effect of side grooves			
CT10	49.1	0.0120	0.050	Effect of side grooves			
CT11	49.2	0.0115	0.100	Effect of side grooves	0.259	0.201	90.0
CT12	49.2	0.0110	0.100	Effect of residual stress	0.213	0.161	92.0
CT13	49.2	0.0080	0.100	Effect of residual stress	0.222	0.280	9.0
CT14	49.1	0.0060	0.100	Effect of residual stress	0.270	0.320	8.0
CT15	49.2	0.0085	0.100	0.1 inch growth, test accuracy of compliance	0.108	0.151	6.0
CT16	49.2	0.0085	0.100	Effect of residual stress	0.256	0.325	6.0
CT17	---	---	0.100	Baseline toughness	0.251	0.268	60.0
CT18	---	---	0.100	0.1 inch growth, test accuracy of compliance	0.109	0.136	60.0
CT19	---	---	0.100	0.014 inch CMOD, test accuracy of compliance	0.011	0.025	
CT20	49.2	0.0105	0.100	PT, NO TEST, fatigue open			
CT22	49.2	0.0100	0.100	Effect of residual stress	0.261	0.208	92.0
CT23	49.2	0.0115	0.100	0.1 inch growth, test accuracy of compliance	0.186	0.125	92.0
CT24	49.2	0.0120	0.100	Effect of residual stress	0.319	0.281	102.0
CT25	49.2	0.0082	0.100	Effect of residual stress	0.259	0.335	7.0
CT26	49.2	0.0105	0.100	NO TEST--just fatigue open			
CT27	49.2	0.0090	0.100	Effect of residual stress	0.260	0.347	6.0
CT28	49.2	0.0100	0.100	0.050 inch growth, test accuracy of compliance	0.053	0.164	7.0
CT29	49.2	0.0092	0.100	0.007 inch CMOD, test accuracy of compliance	0.032	0.112	5.0
CT30	41.0	0.0032	0.100	Effect of residual stress	0.202	0.235	19.0
CT32	49.2	0.0089	0.100	0.003 inch CMOD, test accuracy of compliance	0.005	0.052	
CT33	49.2	0.0128	0.100	0.0165 inch CMOD, test accuracy of compliance	0.091	0.020	
CT34	41.0	0.0033	0.100	Effect of residual stress	0.268	1.280	74.0
CT35	49.2	0.0112	0.100	NO TEST, fatigue open			
CT36	41.0	0.0031	0.100	NO TEST, fatigue open			
CT45	49.2	0.0145	0.100	Effect of residual stress	0.380	0.318	94.0
CT46	49.2	0.0105	0.100	Effect of residual stress	0.304	0.247	89.0
CT47	49.2	0.0125	0.100	0.1 inch growth, test accuracy of compliance	0.141	0.076	95.0
CT48	49.2	0.0120	0.100	0.1 inch growth, test accuracy of compliance	0.157	0.083	101.0
CT49	---	---	0.100	0.1 inch growth, test accuracy of compliance	0.074	0.096	60.0
CT50	41.0	0.0024	0.100	PT, NOT TEST, fatigue open			
CT51	41.0	0.0025	0.100	Effect of residual stress	0.262	0.306	21.0
CT52	41.0	0.0025	0.100	0.040 inch growth, test accuracy of compliance	0.045	0.065	24.0
	Tensile Residual Stress						
	Baseline						
	Compressive Residual Stress						

created through testing. Specimen fracture surfaces were photographed. Analyzed test data is plotted as crack driving force J (a measure of elastic-plastic fracture toughness) versus crack extension. While mechanical testing was progressing, finite element analyses were conducted on each specimen independently from the mechanical testing to avoid influence of results.

For the purposes of this report, an initiation toughness J_{Ic} is defined as the crack driving force at 0.008 inch of crack extension. Values of J_{Ic} reported herein do not conform to the validity requirements of ASTM E1820 [5] because of the effect of residual stresses on the compliance crack length measuring method.

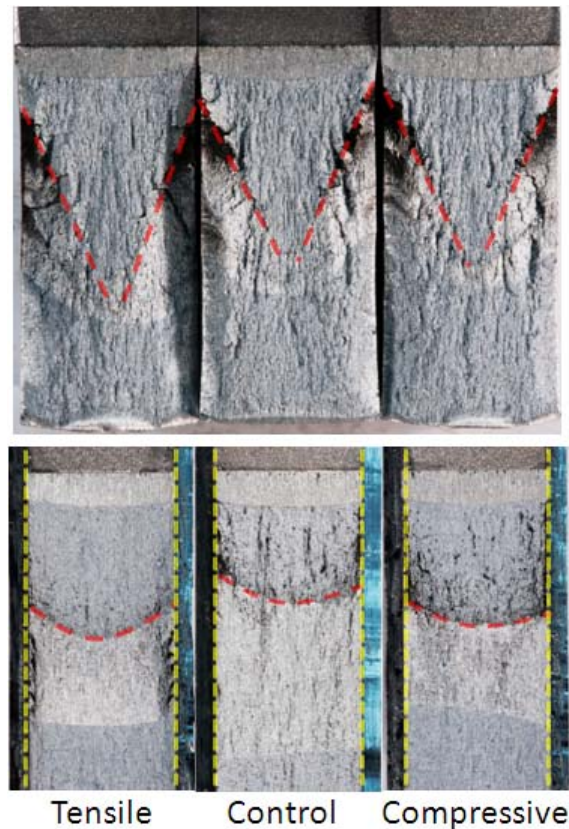


Figure 16: Photographs of specimen fracture surfaces with no side grooves (top row) and 20% side grooves (bottom row). In each, the crack grows toward the bottom of the page. Ductile crack fronts are highlighted in red and net thickness due to side grooves highlighted in yellow.

Initial testing was conducted on specimens with no side grooves, followed by specimens with side grooves corresponding to 10% of the thickness, and the majority of testing was conducted on specimens with side grooves corresponding to 20% of the thickness. The machining of side grooves is a standard practice allowed by ASTM E1820 [5] of removing a narrow V-shaped channel on each face along the crack path that increases the crack front straightness by providing more uniform stress intensity through the thickness of the specimen. Straight crack fronts ensure an acceptable level of accuracy in the compliance technique for measurement of crack length.

Figure 16 shows the resulting fracture surfaces of specimens without side grooves compared to specimens with 20% side grooves. Non-side grooved specimens exhibited significant crack tunneling (pointed crack fronts). Specimens with the 20% side grooves have crack fronts that are slightly curved, but considered acceptably straight according to ASTM E1820 [5].

The analyses described in the following sections are conducted with 3D Abaqus/Explicit finite element codes and utilizes the I_1 - J_2 - J_3 plasticity model and the Lode parameter-dependent ductile fracture model detailed above. Finite element analyses of this study are evaluated by comparing the load-displacement curves and resulting fracture surface profiles generated in the analyses with those generated during the mechanical testing. The observation that the models

can accurately predict the load-displacement records of the experimental tests and the shape and extent of the crack growth is taken as verification of the validity of the computational models.

3.1. Analysis of Control Specimen with No Side Grooves

The plane-sided specimen with no applied residual stress was modeled as a baseline to determine the effect of side grooves.. The element size of the quarter-symmetry model along the crack path is 0.010 inch in all three directions. Eight-node, isoparametric, brick elements with reduced integration are used in the analysis. Figure 17 shows the quarter-symmetry finite element mesh and a close-up of the crack tip region with the crack growing to the right.

The computed and measured load-displacement curves of the plane-sided specimen are compared in Figure 18. Good agreement is observed before fracture initiation at the peak of the curve. The simulation slightly under-predicts the applied force at the end of the crack extension. Figure 19 compares the predicted crack profile with the fracture surface of the broken specimen and the agreement is very good, giving confidence in the fidelity of the computational model. In particular, a “V” shaped crack profile is observed in both test and simulation results, showing significant crack tunneling, which is due to the variation of the stress triaxiality in the thickness direction. Figure 19 (right) displays the stress triaxiality contour on the crack plane, illustrating that high stress triaxiality in red decreases from the mid-plane to the sides.

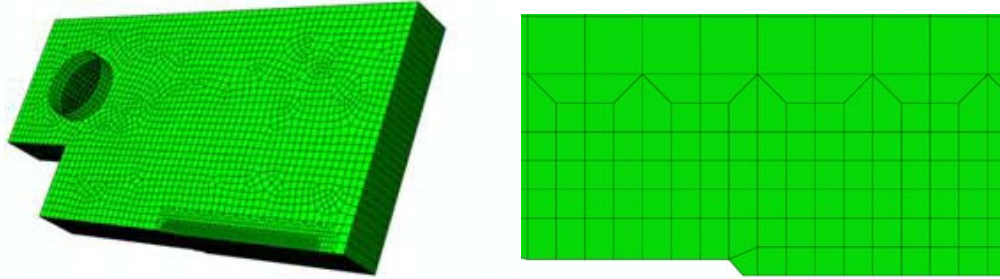


Figure 17: Finite element mesh of the control specimen, no side grooves.

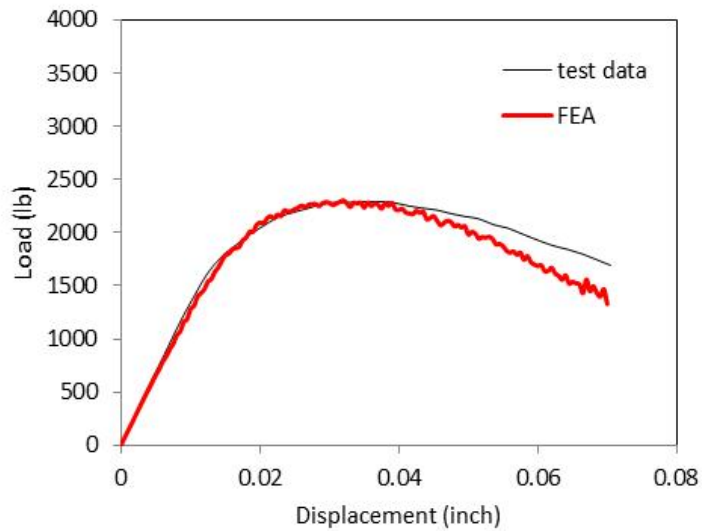


Figure 18: Comparison of computed and measured load-displacement curves of the control specimen, no side grooves.

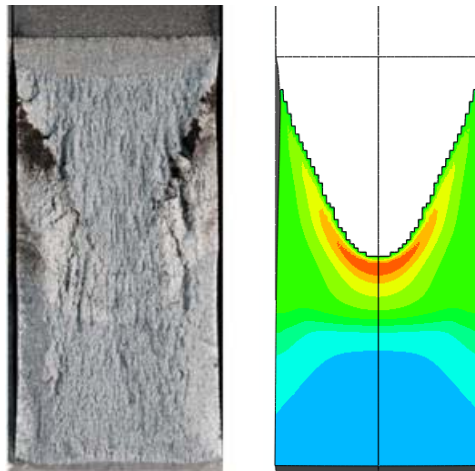


Figure 19: Fracture surface and stress triaxiality distribution in the control specimen, no side grooves.

3.2. Analysis of Control Specimen with 20% Side Grooves

As indicated above, the majority of specimens are side-grooved by 20% of the thickness (10% each side) to obtain more uniform through-thickness crack growth. A quarter-symmetry finite element model was generated for the side-grooved specimen in which the same element type and size are used as those for the plane-sided specimen. With the side grooves, the constraint level is significantly raised near the specimen edges and as a result, more uniform crack growth (less tunneling, corresponding to a straighter crack front) is observed.

Figure 20 (left) compares the predicted crack profile with the crack surface of the broken specimen. Figure 20 (right) demonstrates that stress triaxiality becomes almost uniform through specimen thickness due to the side grooves.

Figure 21 compares the load-displacement curves for the side-grooved specimen with that of the plane-sided specimen. The load carrying capacity of the specimen is significantly reduced by the side grooves. The model predicted load-displacement curves are also included in Figure 21, showing good agreement with test data. The predicted crack growth is compared with experimental measurements at the same applied load levels, displaying good agreement between the two. As with the plane-sided specimens, the analysis of the side-grooved specimen slightly underestimates the load at the final crack extensions.

The experimental crack extension for the two side-grooved control specimens (specimens with no applied residual stress) CT17 and CT18 was compared to the computationally predicted final crack extension at the corresponding load-displacement point. CT17 has a final crack extension of 0.268 inch measured optically from its fracture surface compared to 0.280 inch predicted by the analysis. CT18 has a final crack extension of 0.136 inch measured optically from its fracture surface compared to 0.110 inch predicted by the analysis. The finite element analyses predict the amount of crack extension in the control specimens well, adding confidence in the accuracy of the model.

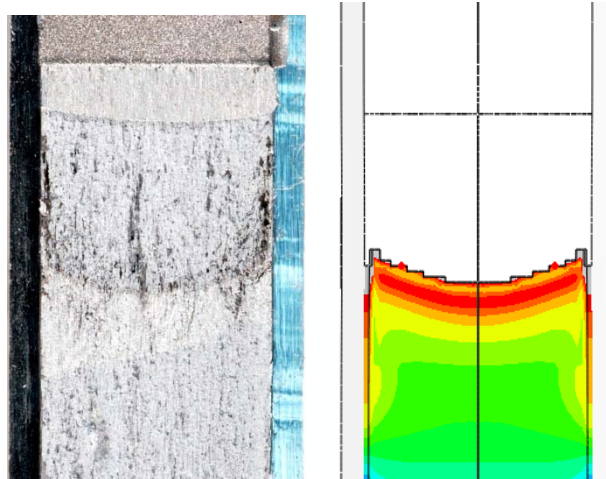


Figure 20: Fracture surface and stress triaxiality distribution in the side-grooved specimen.

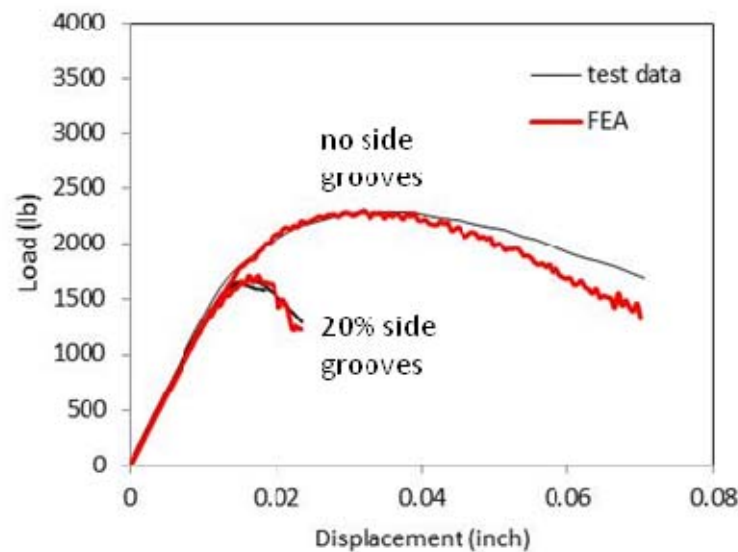


Figure 21: Comparison of the load-displacement curves for side-grooved and plane-sided specimens.

3.3. Tensile Residual Stress Testing

Side compression was applied ahead of the crack tip to impart a tensile residual stress state at the crack tip. Two levels of residual stress were tested based upon the amount of side compression applied to the specimens. In attempting a nominal 0.006 inch side compression per side (0.012 inch total), the press was loaded to its capacity of 49 kip, resulting in an average total side compression of 0.010 inch. Additional tests were conducted at a lower total side compression using an applied load of 41 kip, resulting in an average total side compression of 0.003 inch. Specimens with an average total side compression depth of 0.010 inch were compared to specimens with an average total side compression depth of 0.003 inch and both of these sets

were compared with the uncompressed control specimens. Figure 22 illustrates the effect of applied tensile residual stress on the elastic-plastic toughness J of the specimen. With increased side compression depth, applied residual stress increases and effective toughness decreases. As shown in the 0.010 inch side compressed specimens, initiation toughness is very low; the average J_{Ic} is 7.0 in-lb/in² compared to the control specimen average initiation toughness of 60.4 in-lb/in², which is an 88% reduction in toughness. The tensile residual stresses generated by the 0.003 inch side compression resulted in an average initiation toughness of 21.3 in-lb/in², which is a 74% reduction in toughness compared to the control specimen average.

Due to the low toughness measured and crack length estimate differences between the end of precracking and the start of the fracture toughness test, it was suspected that the applied tensile residual stress specimens that had undergone the more intense side compression experienced crack extension during the side compression process. To investigate if cracking was initiating during the side compression process due to the application of tensile residual stress, three specimens were side compressed at total depths of 0.003 inch (specimen CT50), 0.011 inch (specimen CT20), and 0.011 inch (specimen CT26). Without testing the specimens, they were subjected to fatigue loading at low elastic stresses so that the resulting fracture surface would be highlighted by distinct regions of potential crack initiation and subsequent fatigue.

Figure 23 presents the fracture surfaces of the three specimens. The horizontal line at the bottom of each specimen in the photo represents the tip of the initial machined notch and the smooth region above the notch tip is the fatigue precrack region, whose upper extent is the smooth arc. Beyond the smooth precrack, a darker, rougher region can be seen in specimens CT20 (center) and CT26 (right), which were compressed to the typical total compression depth of 0.010 inch. This darker region is ductile crack extension resulting from the side compression process. The lesser amount of total side compression (0.003 inch) applied to specimen CT50 (left) resulted in no discernible crack extension. The region beyond the faintly visible precrack in specimen CT50 is crack extension due to the post-side compression fatigue and is expectedly similar in appearance to the fatigue precrack region.

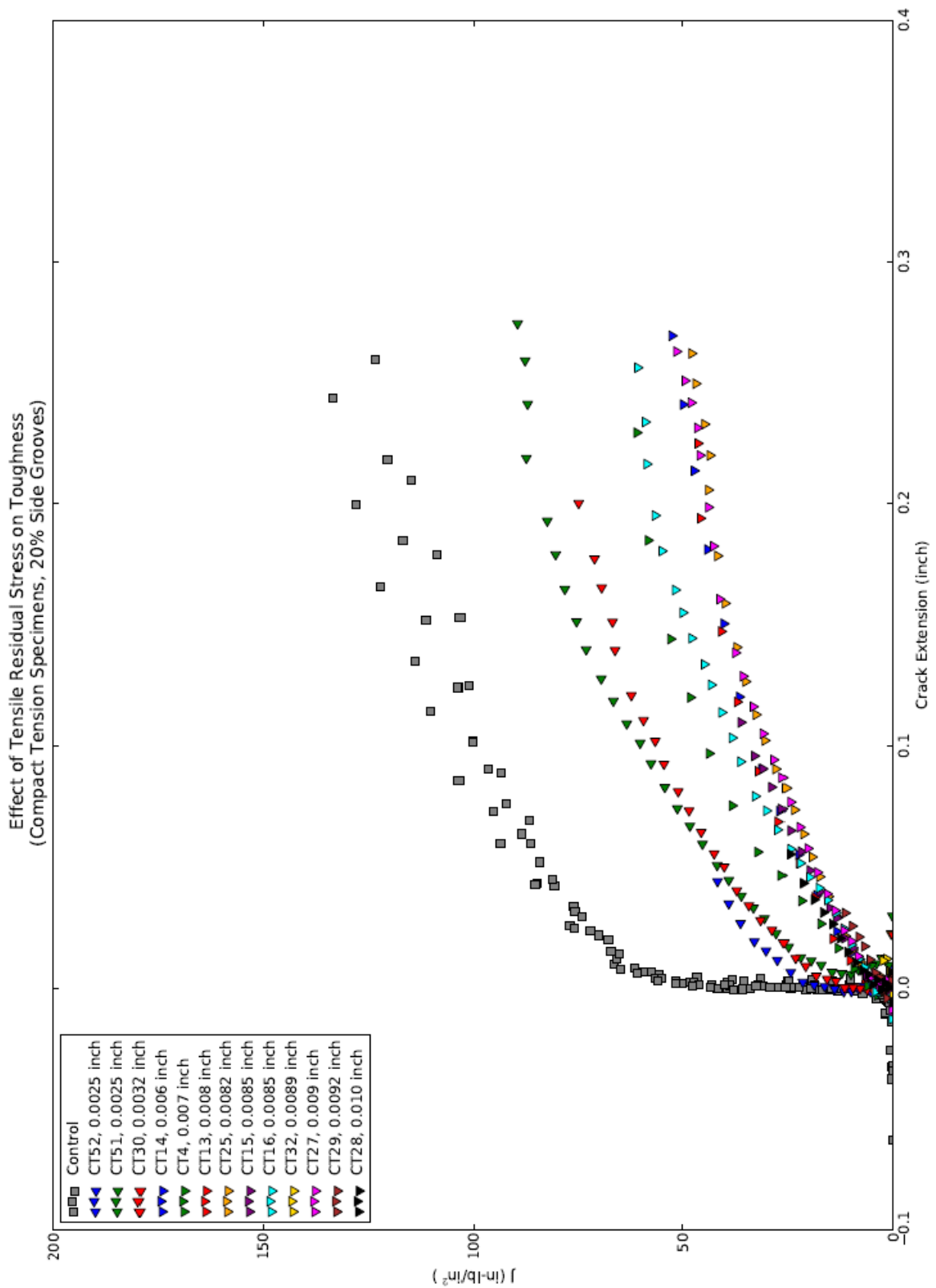


Figure 22: Crack driving force J versus crack extension for control specimens and applied tensile residual stress specimens.

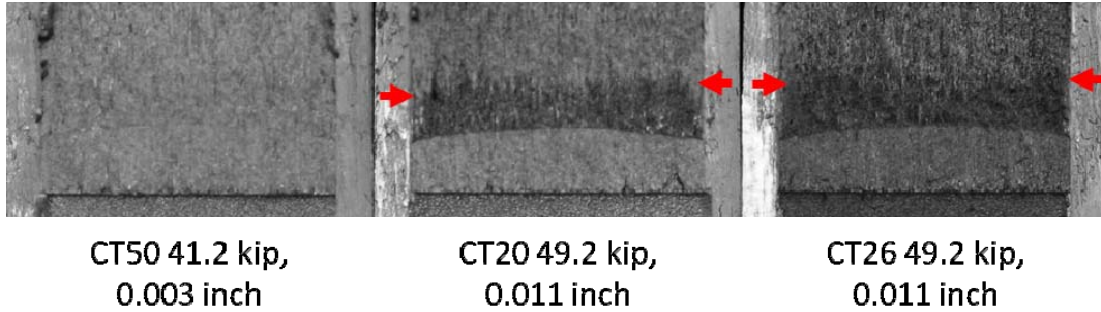


Figure 23: Photographs of fracture surfaces of applied tensile residual stress specimens that were side compressed, followed by fatigue separation; no toughness test was conducted. In each, the crack grows toward the top of the page and the extent of side compression induced crack extension is darkened by dye penetrant and indicated with arrows.

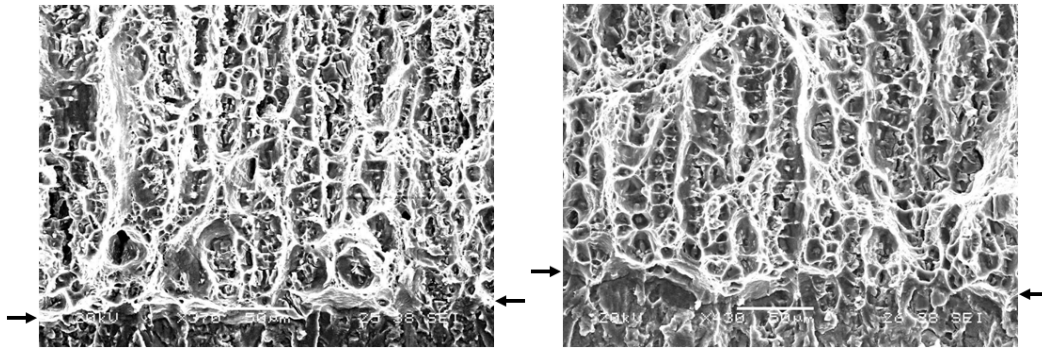


Figure 24: SEM micrographs of fracture surface of applied tensile residual stress specimen CT26 with 0.011 inch side compression followed by immediate fatigue (left) and a tested control specimen CT17 (right). In each, the crack grows toward the top of the page and the transition from the fatigue precrack to ductile tearing is indicated.

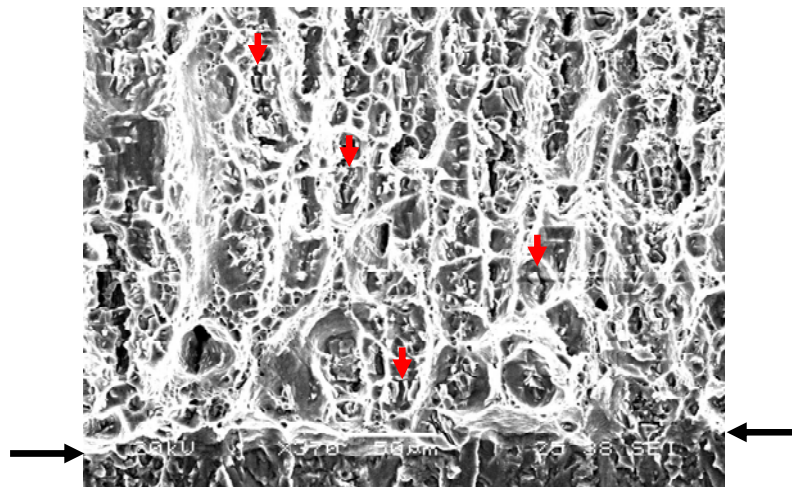


Figure 25: SEM micrograph of fracture surface of applied tensile residual stress specimen CT26 with typical cracked inclusions indicated with vertical arrows. The global crack grows toward the top of the page and the transition from the fatigue precrack to ductile tearing is indicated with horizontal arrows.

Scanning electron microscope (SEM) imaging of applied tensile residual stress specimen CT26 (0.011 inch side compression), on the left in Figure 24, displays evidence of ductile tearing beyond the fatigue precrack in the elongated voids that dominate the upper region of the image. This ductile tearing is identical in appearance to that of control specimen CT17, pictured to the right, which was tested according to the normal procedure. The ductile tearing present in the untested specimens at the higher level of applied residual stress is further evidence that initiation unexpectedly resulted from the side compression process.

In addition to the ductile crack extension along the crack path, SEM imaging revealed cracked inclusions within microvoids on the fracture surfaces on all specimen configurations. In the control specimens, the applied compressive residual stress specimens, and the 0.003 inch nominal side compression tensile residual stress specimens, the crack plane normals of these fractured inclusions are oriented along the global crack path, consistent with the stresses applied during fracture testing. However in the applied tensile residual stress specimens with the 0.010 inch side compression, fractured inclusions found in the ductile crack extension created by side compression had crack plane normals oriented parallel to the axis of the side compression, such as those highlighted in Figure 25. Microcracks in this orientation were not observed in the other specimens. Dual side compression indents straddled the crack path on these specimens with the intention of preventing damage in the crack path, but as observed, this was not the case with the 0.010 inch side compression in the tensile configuration.

Despite the failure to experimentally isolate the residual stress from this damage in the specimens of this configuration, the computational model, described below, captures this undesired damage and crack extension, resulting in analyses that agree well with the experiments.

3.4. Analysis of Tensile Residual Stress Specimens

In the finite element analysis, the first step is to model the side compression process. The cylindrical punches are modeled as rigid surfaces with a friction coefficient of 0.001 (almost frictionless) between the punch and the specimen surface. The rigid punch is pressed into the side of the specimen under displacement control (the standard method in Abaqus/Explicit) according to the residual stress configuration. When the reaction force reaches the level of the experimental applied side-compression load, the punch is removed, leaving the side-compression indents.

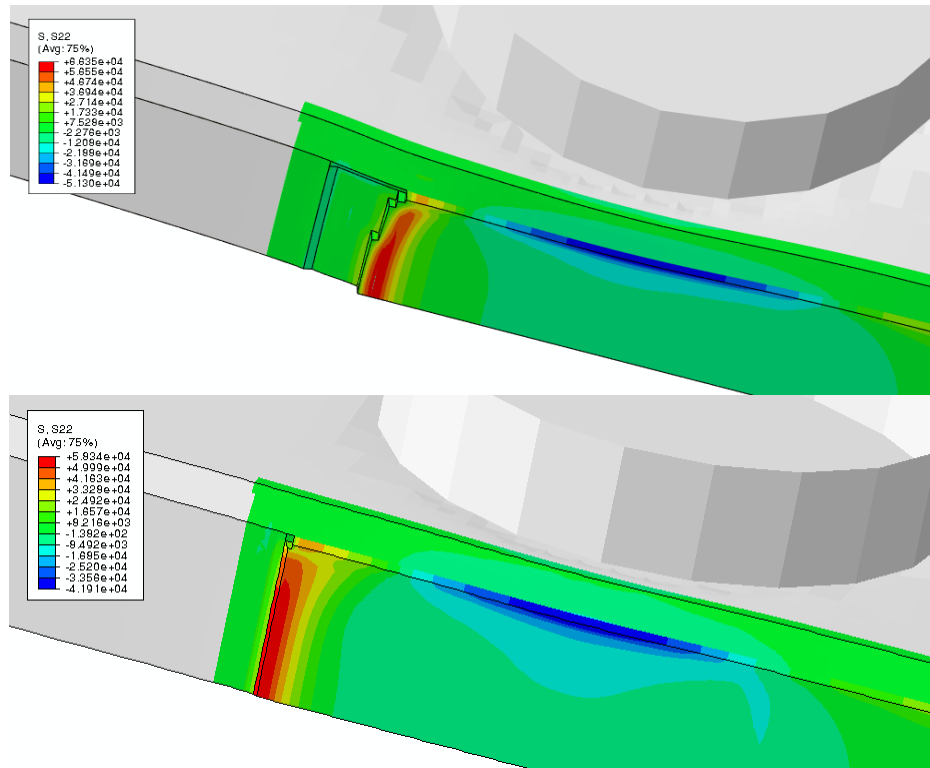


Figure 26: Contour plots of the residual stress normal to the crack plane, 49 kips side-compression (top) and 41 kips side-compression (bottom).

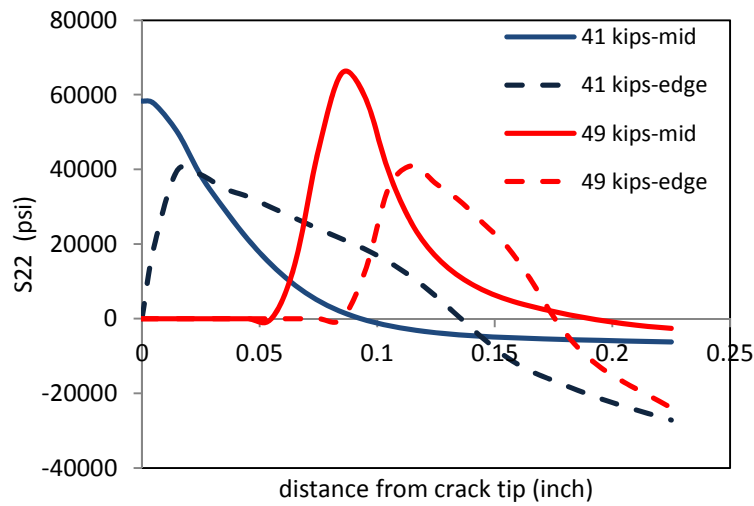


Figure 27: Residual stresses (σ_{22}) distributions ahead of the crack tip at the mid-plane and the specimen edge.

Two values of side-compression forces, 41 kips and 49 kips, were used in the experiments to generate two levels of tensile residual stresses. The average total indentation depths (after the punches were removed) are 0.003 inch and 0.010 inch for 41 kips and 49 kips, respectively. The finite element analyses result in 0.004 inch and 0.009 inch total indentation depths following applied loads for these two cases, showing good agreement with the experimental procedure.

The simulation results for both levels of side compression agree with the test observations. Figure 26 shows the crack front region after side compression with the crack growth direction oriented to the right. The upper image shows the 0.010 inch side compression condition and the resulting crack extension highlighted by the stepped appearance (created by the remaining elements after the adjacent elements were deleted during the numerical crack growth procedure) and the red contour of residual stress normal to the crack plane. The analysis indicates that the crack indeed extends about 0.060 inch for the 0.010 inch side compression condition, while no significant crack extension was observed in the analysis of the 0.003 inch side compression condition.

The contours of residual stresses normal to the crack plane are also shown in Figure 26. The high positive residual stress is confined in a small region close to the crack tip, within about 0.050 inch from the crack tip for both the 0.010 inch (top image) and 0.003 inch (bottom image) side compression depths. Figure 27 displays the variation of the crack plane normal component of residual stress, σ_{22} , ahead of the crack front after the side compression punch has been removed. The peak tensile residual stress σ_{22} generated by the 0.010 inch side-compression is 66 ksi, corresponding to a von Mises equivalent stress of 33 ksi, which reaches the material yield strength of 32.3 ksi and confirms that this side compression depth applies yield-level residual stresses to the specimen. The peak tensile residual stress σ_{22} generated by the 0.003 inch side compression is 59 ksi, corresponding to a von Mises equivalent stress of 24 ksi, which is 74% of the average measured yield strength.

3.5. Compressive Residual Stress Testing

Residual stress was applied behind the crack tip to impart a compressive residual stress state. Two levels of residual stress were tested based upon the amount of side compression applied to the specimens. Specimens with an average total side compression depth of about 0.012 inches, generated with an applied load of 49 kip, were compared to specimens with an average total side compression depth of about 0.003 inches, generated with an applied load of 41 kip, and the control specimens. Figure 28 illustrates the effect of applied compressive residual stress on toughness. The effect of compressive residual stress effectively increases the toughness of the specimen relative to the control data. With increased side compression depth, residual stress increases and the effective toughness increases. The specimens with the 0.012 inch of side compression have an average initiation toughness of 94.2 in-lb/in², which is an increase of an average of 56% over the average toughness for control specimens of 60.4 in-lb/in². The specimen with 0.003 inches of side compression has an initiation toughness of 74.0 in-lb/in², which is an increase of 23% over the average toughness for control specimens.

Since the residual stress applied through side compression alone initiated crack extension in the tensile configuration, this phenomenon was also tested in the compressive configuration. Side

compression was applied in the compressive residual stress configuration to a specimen at a total depth of 0.003 inches and to another specimen at 0.011 inches. As with the specimens in the tensile configuration, these specimens were subjected to low stress fatigue without testing in order to break the specimen open for observation. The photographs presented in Figure 29 both show the edge of the fatigue precrack (crack growth pointing upwards), followed directly by the post-side compression fatigue. As expected, neither fracture surface showed evidence of ductile crack extension initiating at the edge of the fatigue precrack, suggesting that the side compression of these specimens itself does not cause crack extension or impart damage to the underlying material along the crack path, unlike the higher level of applied tensile residual stress. The effect of compressive residual stress is effectively isolated.

3.6. Analysis of Compressive Residual Stress Specimens

Finite element modeling of the side-compression process to generate compressive residual stress is slightly different from the tensile residual stress case. When side-compression is applied behind the crack tip, the crack closes, and the crack surfaces contact each other. To prevent crack surface penetration in the model, a rigid surface is added to the pre-cracked area along the initial crack plane. Analysis results show that the high compressive residual stress region is at the initial notch (behind the fatigue pre-crack front) and located on the surface of the specimen, Figure 30 (left). Figure 30 (right) shows the variation of the residual stress (σ_{22}) with the distance in the crack growth direction (the crack tip is at $x = 0$) at the mid-plane. The von Mises equivalent of the peak applied compressive residual stress calculated for the 0.012 inch side compression is 31.6 ksi, which is essentially equivalent to the average measured yield strength of 32.3 ksi. The von Mises equivalent of the peak applied compressive residual stress calculated for the 0.003 inch side compression is 27.2 ksi, which is 84% of the average measured yield strength.

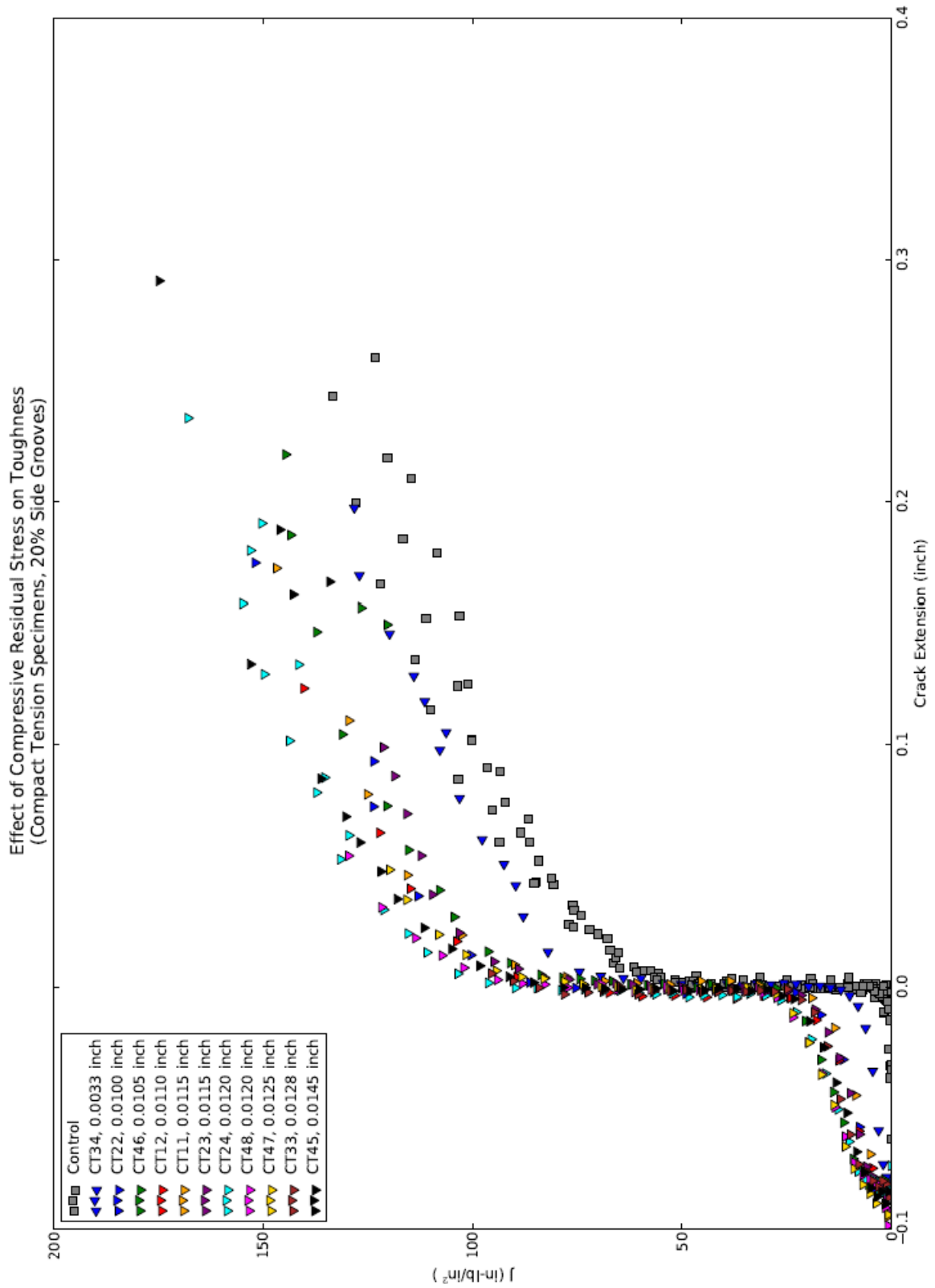


Figure 28: Crack driving force J versus crack extension for control specimens and applied compressive residual stress specimens.

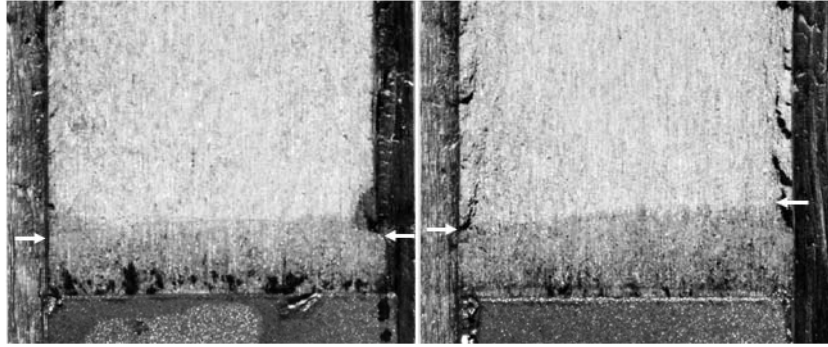


Figure 29: Photographs of fracture surfaces of applied compressive residual stress specimens CT35 with 0.011 inch of side compression (left) and specimen CT36 with 0.003 inch of side compression (right). In each, the crack grows toward the top of the page and the edge of the fatigue precrack is indicated.

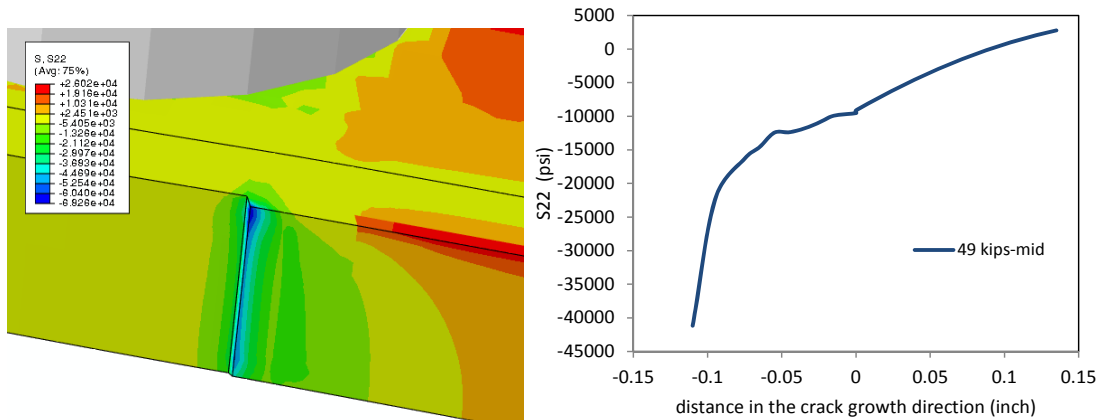


Figure 30: Contour plot of the residual stress normal to the crack plane at the initial notch with the crack growth direction to the right (left) and plot of the variation of residual stress (σ_{22}) with the distance in the crack growth direction (right).

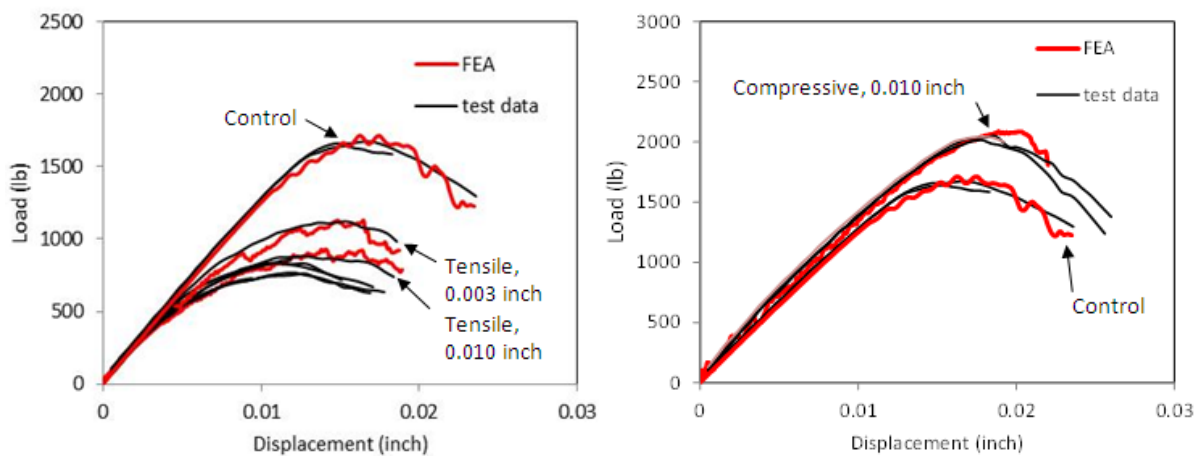


Figure 31: Comparisons of the computed and measured load-displacement curves for applied tensile residual stress (left) and applied compressive residual stress (right).

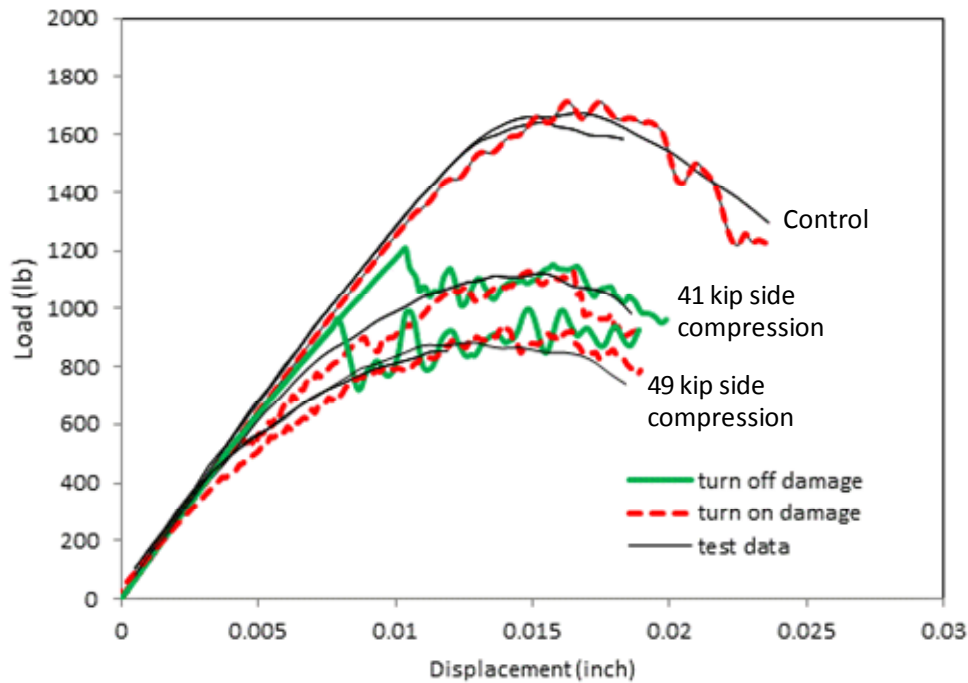


Figure 32: Load-displacement response comparing FEA of applied tensile residual stress specimens with the control specimen to isolate the effect of damage from residual stress.

3.7. Separating the Effects of Side Compression from Plastic Damage and the Effects of Residual Stress on Fracture Toughness

Results of both testing and analysis shows that side compression generates substantial residual stresses, but it also damages the microstructure ahead of the crack and in the extreme can cause crack extension. The Gao et al. model accurately predicts the combined effects of these components, but it is difficult to uncouple the effects to determine the component of toughness decrease that is due solely to residual stress. Figure 32 compares the final load-displacement responses when damage accumulation is “turned on” or “turned off” during the side compression process. Disabling damage accumulation creates numerical issues and is the cause for the oscillations. Even so, the figure clearly indicates that reduction of fracture resistance can be mainly attributed to the effect of residual stress. The damage that resulted from the side compression only affects crack initiation and the initial part of the curve, prior to the sharp drop in load. After the crack grows some amount, the predicted load-displacement curve is similar no matter whether damage accumulation was turned on or off during the side compression process. For the compressive residual stress configuration there is no effect of the side compression on the fracture toughness test results since, in this case, the side compression is remote from the fracture process zone and does not result in any microstructural damage that affects the subsequent fracture toughness test.

4. Discussion

Flaw tolerance refers to a material's ability to resist fracture and can be quantified as a geometry-independent ratio $\frac{K_r}{S_r} \cdot \frac{K_{mat}}{\sigma_y}$, where K_r is the ratio of elastic crack driving force (in other words, stress intensity) to total crack driving force, S_r is the ratio of applied stress to yield stress, K_{mat} is the linear elastic material toughness (in this case K_{Ic}), and σ_y is the material yield strength. When the applied crack driving force is entirely elastic and the applied stress reaches yield, the flaw tolerance ratio becomes the toughness ratio K_{Ic}/σ_y . The toughness ratio is used by the US Navy's Fracture Toughness Review Process [11] for critical applications and is derived from the pressure vessel and power industries' practices of determining fitness of service for flawed components. It is a geometry-independent parameter that allows material testing on a laboratory scale to translate to ship structure. The toughness ratio is used as a minimum value in design when selecting materials for fracture resistance. Theoretically, if the toughness ratio of a material is below one, a crack will extend from a flaw under elastic stresses. In practice, when the Fracture Toughness Review Process is invoked, the US Navy requires a minimum toughness ratio of 1.15, which is based on historical data and additional factors. The material sample of this study, 5083-H116 aluminum, has a toughness ratio (based on the average values of elastic-plastic fracture toughness converted to linear-elastic fracture toughness measured from the control specimens and the average measured yield strength) of $29.67 \text{ ksi}\sqrt{\text{in}} / 32.3 \text{ ksi} = 0.92$. A toughness ratio measured for this plate that is less than one suggests that 5083-H116 will crack under elastic stresses.

This study applied yield-level tensile residual stresses to 5083-H116 and through testing and analysis, demonstrated that effective toughness is drastically reduced. Reducing the material toughness reduces the toughness ratio, meaning that even lower elastic stresses are required to initiate fracture. Experiments verified that fracture occurred during the application of residual stresses without additional loading.

5. Conclusions

The average measured elastic-plastic fracture toughness of 5083-H116 in the T-L orientation from specimens with no applied residual stress is $J_{Ic} = 60.4 \text{ in-lb/in}^2$. The average measured elastic-plastic fracture toughness for an applied equivalent yield-level tensile residual stress of 33 ksi is 7.0 in-lb/in^2 and 21.3 in-lb/in^2 for an applied equivalent tensile residual stress of 24 ksi. The average measured elastic-plastic fracture toughness for an applied equivalent yield-level compressive residual stress of 31.6 ksi is 94.2 in-lb/in^2 and 74.0 in-lb/in^2 for an applied equivalent compressive residual stress of 27.2 ksi.

Applied yield-level tensile residual stress plus the microstructural damage due to the side compression process reduced the initiation toughness by an average of 88%. Applied tensile residual stress equivalent to 74% of yield reduced the initiation toughness by an average of 65%.

The application of yield-level tensile residual stress alone initiated ductile crack extension. This was confirmed by optical and electron microscopy of specimen fracture surfaces that were side compressed, but not tested. Corresponding finite element analysis exhibited a similar amount of

crack extension as the experiments. The application of sub-yield tensile residual stresses alone did not introduce measurable crack extension, as confirmed by fracture surface inspection. Corresponding finite element analysis of the side compression process at this applied residual stress level also did not exhibit crack extension.

Applied yield-level compressive residual stress increased the initiation toughness by an average of 56%, while applied compressive residual stress equivalent to 84% of yield increased the initiation toughness by 23%. Finite element analyses using the presented plasticity and fracture model closely predicted crack initiation and extension in all cases. The finite element analyses were verified by comparison of predicted with experimental load-displacement response and comparison of predicted with experimental crack front appearance.

The application of compressive yield-level and sub-yield residual stresses alone did not initiate ductile crack extension, as confirmed by optical inspection of specimen fracture surfaces. Corresponding finite element analysis of the side compression process also did not exhibit crack extension.

Residual stresses have significant effects on elastic-plastic fracture initiation toughness J_{Ic} and elastic-plastic crack extension. This study's methodology introduces residual stresses, but introduces significant microstructural damage for the yield-level tensile residual stress case. The presented plasticity and fracture model accounts for this damage. Total experimental separation of the effects of damage from the applied residual stress was not possible, though work in this pursuit suggested that the residual stresses were the larger contributor to the reduction in fracture toughness in the case of tensile residual stresses. In the case of compressive residual stresses, microstructural damage due to the side compression process had little to no effect on the measured effective fracture toughness elevation.

6. Implications for Ship Structure

Two unavoidable phenomena plague welded ship structure—fatigue crack initiation and the introduction of residual stress via welding. Although resistance to fatigue crack initiation is a primary design requirement in much of ship structure, real world imperfections such as material and weld defects, sharp corners, and corrosion are inevitable and provide initiation sites for cracks. Additionally, the contraction of weld metal as it cools introduces residual stresses (which can be as high as the material yield strength) in the less tough material local to the weld. Fatigue cracks in the presence of residual stresses are a recipe for fracture, especially for materials like 5083-H116 that are susceptible to fracture in the presence of cracks under elastic stresses. This study suggests that residual stresses in welded 5083-H116 ship structure can drive ductile crack extension under little or no elastic stresses.

Effort can be expended to either prevent or manage fracture of aluminum ship structure, and as always is a balance between economics and damage tolerance. The increased effective toughness due to applied compressive residual stress measured in this study demonstrates the potential of targeted compressive structural surface treatments such as peening to improve

fracture resistance. Local heat treatment of ship structure is another method for relief of residual stresses.

These methods are costly and, for maximum effect and to limit cost, require a detailed answer to the age-old question: What exactly is the level of residual stress in my structure? In situ residual stress measurement techniques can provide acceptable measurements, but are also costly and are often destructive tests. Most full scale ship structural finite element models are not currently sufficiently detailed to provide an accurate understanding of the complex residual stress fields at play. Successive analyses with focused refinements traversing the length scale from the shell elements of a full size ship down to individual analyses of structural hot spots with the resolution of three dimensional elements at a crack tip while applying a model such as the one presented is an approach to effectively model welds and residual stresses for more accurate predictions of structural fracture. These high fidelity analyses can be used to optimally locate welded joints to minimize residual stresses and associated cracking.

Determination of critical flaw sizes calculated with the effective toughness of structures in light of residual stresses combined with non-destructive evaluation techniques and inspection intervals based upon fatigue crack growth rates establish the basis for a fracture control plan. Such plans wisely tolerate cracks and inform decision makers on how long a crack can grow before structural repair or replacement is necessary.

7. Recommendations for Future Research

This study is a starting point to more effectively managing the effects of residual stresses on ship structure. Increased investment in modeling of residual stresses will enable more accurate predictions of structural fracture and fatigue. Although the presented model predicts fracture in laboratory coupon specimens, experimental validation using structural elements is the next step in reinforcing the model's applicability. A laboratory-scale aluminum structural weld detail of interest can be fabricated, a crack can be introduced, and various levels of residual stress can be mechanically applied during structural loading and compared with the as-welded specimen. Independently, the experiment can be modeled utilizing the presented plasticity and fracture model to evaluate its applicability to structure.

The coupled experimental-analytical approach of this study can also be applied to back-calculate residual stress states from cracked specimens. Unknown residual stresses can be applied to an alternate fracture specimen such as a single edge bend specimen through the side compression process and the resulting toughness can be measured. Corresponding finite element analyses could model the test to calculate the amount of residual stress present. Hole-drilling techniques could be used to quantify the residual stress levels in untested specimens.

While this study examined ductile crack extension, future research could extend into the realm of fatigue crack growth. Compact tension specimens could be side compressed for different levels of applied residual stress and fatigue crack growth testing could be conducted. Simultaneously, fatigue crack growth can be implemented in the model and used to predict the growth response. A model with this capability is quite useful in determining inspection intervals of cracks in structure.

8. References

- [1] Gao, X., Zhang, T., Hayden, M. and Roe, C. (2009) Effects of the Stress State on Plasticity and Ductile Fracture of an Aluminum 5083 Alloy. *International Journal of Plasticity*, **25**, 2366–2382.
- [2] Gao, X., Zhang, T., Zhou, J., Graham, S.M., Hayden, M. and Roe, C. (2011) On Stress-State Dependent Plasticity Modeling: Significance of the Hydrostatic stress, the Third Invariant of Stress Deviator and the Non-Associated Flow Rule. *International Journal of Plasticity*, **27**, 217–231.
- [3] Johnson, G.R. and Cook, W.H. (1985) Fracture characteristics of three metals subjected to various strains, strain rates, temperatures and pressures. *Engineering Fracture Mechanics*, **21**, 31-48.
- [4] Mahmoudi, A.H., Truman, C.E. and Smith, D.J. (2008) Using local out-of-plane compression (LOPC) to study the effects of residual stress on apparent fracture toughness. *Engineering Fracture Mechanics*, **75**, 1516-1534.
- [5] ASTM E1820-09 Standard Method for Measurement of Fracture Toughness. (2009) ASTM International, West Conshohocken, PA.
- [6] Wilkins, M.L., Streit, R.D. and Reaugh, J.E. (1980) Cumulative-strain-damage model of ductile fracture: simulation and prediction of engineering fracture tests, ucrl-53058. Technical report, Lawrence Livermore Laboratory, Livermore, CA.
- [7] Xue, L. and Wierzbicki, T. (2009) Ductile fracture characterization of aluminum alloy 2024-T351 using damage plasticity theory. *International Journal of Applied Mechanics*, **1**, 267-304.
- [8] Li, Y., Wierzbicki, T., Sutton, M.A., Yan, J. and Deng X. (2011) Mixed mode stable tearing of thin sheet al. 6061-T6 specimens: experimental measurements and finite element simulations using a modified Mohr-Coulomb fracture criterion. *International Journal of Fracture*, **168**, 53-71.
- [9] Abaqus/Standard User's Manual (version 6.9), SIMULIA, Providence, RI, 2008.
- [10] Kim J, Gao X. (2005) A generalized approach to formulate the consistent tangent stiffness in plasticity with application to the GLD porous material model. *International Journal of Solids and Structures*, **42**,103-22.
- [11] Fracture Toughness Review Process for Metals in Critical Non-Nuclear Shipboard Applications. (1998) Naval Sea Systems Command, Washington Navy Yard, DC.

SHIP STRUCTURE COMMITTEE LIAISON MEMBERS

LIAISON MEMBERS

American Society of Naval Engineers	Captain Dennis K. Kruse (USN Ret.)
Bath Iron Works	Mr. Steve Tarpay
Colorado School of Mines	Dr. Stephen Liu
Edison Welding Institute	Mr. Rich Green
International Maritime Organization	Mr. Igor Ponomarev
Int'l Ship and Offshore Structure Congress	Dr. Alaa Mansour
INTERTANKO	Mr. Dragos Rauta
Massachusetts Institute of Technology	
Memorial University of Newfoundland	Dr. M. R. Haddara
National Cargo Bureau	Captain Jim McNamara
National Transportation Safety Board - OMS	Dr. Jack Spencer
Office of Naval Research	Dr. Yapa Rajapaksie
Oil Companies International Maritime Forum	Mr. Phillip Murphy
Samsung Heavy Industries, Inc.	Dr. Satish Kumar
United States Coast Guard Academy	Commander Kurt Colella
United States Merchant Marine Academy	William Caliendo / Peter Web
United States Naval Academy	Dr. Ramswar Bhattacharyya
University of British Columbia	Dr. S. Calisal
University of California Berkeley	Dr. Robert Bea
Univ. of Houston - Composites Eng & Appl.	
University of Maryland	Dr. Bilal Ayyub
University of Michigan	Dr. Michael Bernitsas
Virginia Polytechnic and State Institute	Dr. Alan Brown
Webb Institute	Prof. Roger Compton

RECENT SHIP STRUCTURE COMMITTEE PUBLICATIONS

Ship Structure Committee Publications on the Web - All reports from SSC 1 to current are available to be downloaded from the Ship Structure Committee Web Site at URL:

<http://www.shipstructure.org>

SSC 445 – SSC 393 are available on the SSC CD-ROM Library. Visit the National Technical Information Service (NTIS) Web Site for ordering hard copies of all SSC research reports at

URL: <http://www.ntis.gov>

SSC Report Number	Report Bibliography
SSC 466	Mean Stress Assessment in Fatigue Analysis and Design Yuen, B.K.; Koko, T.S.; Polezhayeva, H.; Jiang, L. 2013
SSC 465	Predictive Modeling Impact of Ice on Ship and Offshore Structures Bueno A. 2012
SSC 464	Design and Detailing for High Speed Aluminum Vessels Design Guide and Training Mish, Wh Jr., Lynch T., Hesse E., Kulis J., Wilde J., Snyder Z., Ruiz F. 2012
SSC 463	Marine Composites NDE, Inspection Techniques for Marine Composite Construction Greene, E 2012
SSC 462	Review of Current Practices of Fracture Repair Procedures for Ship Structures Wang, G, Khoo, E., ABS Corporate Technology 2012
SSC 461	Structural Challenges Faced By Arctic Ships, Kendrick A., Daley C. 2011
SSC 460	Effect of Welded Properties on Aluminum Structures, Sensharma P., Collette M., Harrington J. 2011
SSC 459	Reliability-Based Performance Assessment of Damaged Ships, Sun F., Pu Y., Chan H., Dow R.S., Shahid M., Das P.K. 2011
SSC 458	Exact Mapping of Residual Stress in Ship Hull Structures by Use of Neutron Diffraction Das. S. Kenno S. 2009
SSC 457	Investigation of Plastic Limit States for Design of Ship Hull Structures, Daley C., Hermanski G. 2009
SSC 456	Buckling Collapse Testing on Friction Stir Welded Aluminum Stiffened Plate Structures, Paik J.K. 2009
SSC 455	Feasibility, Conceptual Design and Optimization of a Large Composite Hybrid Hull, Braun D., Pejcic M. 2008
SSC 454	Ultimate Strength and Optimization of Aluminum Extrusions, Collette M., Wang C. 2008